TNO Whiffle joint report

TNO 2022 R12060

Towards the use of large eddy simulations for the generation of the atmospheric boundary layer inflow for wind turbine load calculations

Date	20 December 2022
Author(s)	S. Mancini and M. Caboni (TNO), P. Ranka and M. Folkersma (Whiffle)
Copy no	
No. of copies	
Number of pages	47 (incl. appendices)
Number of appendices	0
Sponsor	RvO - grant n.TEHE119043
Project name	AeroLES
Project number	060.43129

Summary

This joint TNO-Whiffle report presents the main results obtained in the third work package of the AeroLES project. The project aims to reduce the uncertainty in the design chain of modern wind turbines by replacing traditional synthetic inflow generation methods with validated wind fields from high-fidelity large eddy simulations (LES) that better resemble reality. Potentially, this would reduce the gap between in-field and simulated inflow conditions enabling better design choices that reduce the cost of the assets.

To reach such an ambitious goal, however, several intermediate steps need to be undertaken. The present work starts by highlighting the main challenges associated with the use of LES for generating the inflow for wind turbine aeroelastic load calculations. The inflow validation challenge is then tackled in Chapter 2, where LES wind field statistics are validated against met mast measurements at two onshore and one offshore sites. The comparison shows a promising agreement overall, with onshore turbulence intensity being subject to higher uncertainty than offshore due to its sensitivity to the surface roughness parameter. Then, to tackle the computational cost challenge and enable efficient LES-based aeroelastic calculations, a software interface that couples Whiffle's LES solver running on Graphical Processing Units (GPU) to a multi-physics simulation tool has been developed (Chapter 3). The tool allows running simulations both in a one-way coupled approach, where the turbine is not modelled in the LES and conventional wake models are used to compute aerodynamic loads, and in a two-way coupled actuator line approach where the turbine wake is modelled in the LES for higher fidelity. Finally, looking for suitable simulation settings and guidelines for using LES in aeroelastic load calculations, a grid sensitivity study is presented in Chapter 4. The power spectral densities of relevant aeroelastic quantities are found to be sensitive to the mesh resolution, not only in the high-frequency part of the spectrum where an energy drop occurs due to spatial filtering, but also at lower nP harmonics where coarse grids appear not entirely able to capture the peaks resulting from the rotational sampling of the turbulence.

The results presented in this report lay the groundwork for the aeroelastic load validation campaign to be carried out in the remainder of the AeroLES project.

Contents

1   Introduction

1.1   Background

With the fast-paced advances in High-Performance Computing (HPC) the attractiveness of high-fidelity numerical tools to model the Atmospheric Boundary Layer (ABL) for wind energy applications has significantly grown. In this context, Large Eddy Simulations (LES) are considered one of the most promising methods to enhance the accuracy of numerically generated wind fields thanks to their ability to directly resolve the turbulence spectrum with the exception of the smallest scales [1].

LES have already quite a long application history in ABL meteorology, mainly focused on the modelling of mesoscale phenomena like atmospheric convection and cloud formation (e.g. [2, 3]). However, the wide range of scales characterizing the troposphere turbulence and the complex interaction between meso- and micro-scale atmospheric phenomena have long prevented ABL LES tools from spreading in the wind energy industry. To effectively model the inflow on a wind turbine indeed, an accurate description of the geostrophic forcing needs to be combined with the resolution of a significant portion of the turbulence spectrum in the surface layer [4]. This entails several orders of magnitude differences between the scales considered [5], imposing the use of large domains combined with strict discretization requirements (in both space and time) and therefore resulting in high computational costs.

Using ABL LES tools to study the inflow on wind turbines may offer valuable advantages, ranging from increased flexibility in modelling site-specific conditions (e.g. complex terrain, stability conditions, wind shear and veer, and diurnal cycles) to the availability of extensive information on turbulence characteristics across large simulation domains that would be difficult to get experimentally [6].

As more powerful HPC solutions reduced the computational burden, in the last decade ABL LES solvers have become more popular in the wind farm aerodynamics research field [1, 7]. Here the turbines are typically modelled as rigid Actuator Discs (AD) or Actuator Lines (AL, [8]), providing a quite accurate description of the far wake evolution [9]. Similar LES-based approaches have been used extensively to study the power production, the wake interaction, and the impact of the ABL stratification for various wind farms (e.g. [10, 11, 12, 13]). Focusing at a farm level the turbulence scales of interest (those affecting the mean power production) are typically quite large and the grid resolution, which drives the Sub-Grid Stress (SGS) filter size as well as the time step duration, can be set accordingly. Although much faster low-fidelity wake models are available in this field (e.g. [14]), high-fidelity ABL LES tools may play an important role in validating and improving such industry-standard methods [7].

Modelling the inflow with ABL LES might have great potential in the context of wind turbine load calculations as well. Load calculations are at the core of the design and certification of any wind turbine and are regulated by the International Electrotechnical Commission (IEC) 61400-1 standard [15], which defines international wind turbine design requirements and prescribes a large set of Design Load Cases (DLCs) to be considered. The standard also defines a Normal Turbulence Model (NTM) that characterizes the inflow turbulence for several DLCs. Two options for the NTM are available: the Kaimal model [16]; and the Mann model [17]. The latter

exploits the rapid distortion theory and eddy lifetime considerations to derive the full wind velocity spectral tensor, whereas the former prescribes non-dimensional velocity component spectra and it is used in combination with an exponential expression for the coherence of the longitudinal component. Several tools that generate synthetic turbulent wind fields for DLC calculations have been developed based on these models (e.g. [18, 19, 20]) and they are widely used by the industry.

Both Mann's and Kaimal's models were developed for homogeneous turbulence in a conventionally neutral ABL, and they do not take into account buoyancy or stratification effects resulting from different stability conditions that are far more common in the field. Although a few extensions of the standard models accounting for ABL stability have been proposed (e.g. [21, 22, 23]) their use is typically limited to research purposes. Another limit of synthetic turbulent wind fields is the lack of site-specific terrain information, as the presence of large obstacles or uneven surface roughness inherently causes inhomogeneities in the inflow turbulence.

The modelling flexibility provided by ABL LES may help overcome the limits of standard synthetic turbulence models. In fact, LES allow taking into account more aspects of the flow physics, from generic ABL stability regimes to site-specific terrain conditions. Potentially, LES-generated wind fields may reduce the gap between in-field and simulated conditions allowing for lower design uncertainty, which would result in better design choices and lower costs. Nevertheless, the use of ABL LES for the generation of turbulent wind fields to perform load calculations is still far from standard practice and many challenges need to be faced to make this a feasible and attractive solution (see Section 1.2).

This work aims to investigate the potential of ABL LES for the generation of realistic wind fields to be used for wind turbine load calculations and to lay the groundwork for an experimental validation study.

1.2   Current challenges and contribution of this work

The best way to assess the value of LES in the generation of the inflow for load calculations is to compare against conventional synthetic wind fields and validate the results with measurements on operating turbines. However, a few important challenges need to be faced before a consistent comparison can be even attempted. The main challenges outstanding, many of which are tackled in this work, can be summarized as follows:

1. **Computational cost**: accurate load calculations require a wide range of turbulence scales to be resolved. The largest eddies combined with the energy-containing integral scales determine the Turbulence Intensity (TI) and the spatial coherence at low wave numbers, hence their modelling is fundamental for both structural loads and power production predictions [5]. Capturing the largest eddies in the surface layer requires rather large domains ($\sim$1-10Km) in which these large vortex structures have to fit. On the other hand, the dynamic behaviour of a turbine is also influenced by eddies in the inertial subrange as the rotational sampling of the turbulence results in a redistribution of the frequency components in the Eulerian spectrum towards different frequency ranges (mostly around rotational speed harmonics) in the rotational spectrum [24]. This phenomenon is of primary importance in aeroelastic load calculations and it requires a fine discretization of the rotor plane to be modelled correctly. The IEC61400-1 standard [15] prescribes tight grid size requirements

for the generation of synthetic turbulent wind fields. Respecting these constraints makes LES simulations computationally expensive. However, with the progress in HPC technology, more efficient ABL LES solvers that run on Graphical Processing Units (GPUs) have been developed allowing major run time reductions [25]. This is how the computational cost challenge is tackled in this work, where a coupling between an aeroelastic solver and a state-of-the-art GPU-based ABL LES software has been developed (Chapter 3).

2. **Inflow validation**: before using LES-generated flow fields for load calculations, the simulation results need to be validated against field measurements in order to gain confidence in their ability to produce realistic wind fields for different sites and atmospheric conditions. The recent works of Mirocha et al. [6] and Peña et al. [26] laid two important stepping stones in this direction inspiring the present work. Here the canonical cases described in [26] have been replicated focusing on the sensitivity of the results to the mesh resolution used in the LES (Chapter 4). Moreover, new inflow validation cases have been considered as described in Chapter 2.

3. **Tools, procedures, and guidelines**: when it comes to detailed load calculations on individual turbines, the use of LES for wind field generation is still far from standard practice. One way to proceed is to follow the conventional Design Load Case (DLC) modelling chain and use the LES software to produce a turbulent wind file, which is then read by the aeroelastic solver just like a standard synthetic wind field [27, 28, 25]. This "offline" approach is inefficient as it requires the generation and handling of large files to link the LES with the aeroelastic solver limiting its applicability to relatively short time histories [25]. Despite a few high-fidelity research tools like the open-source SOWFA (Simulator fOr Wind Farm Applications [29]) coupled with OpenFAST [30] offering the possibility to couple an LES code to an aeroelastic solver, the computational costs entailed limit their use for load calculation purposes and the work from Storey et al. [31] is one of the few publications using an "online" coupling with LES for aeroelastic load calculations. The development of a novel coupling between a state-of-the-art GPU-based ABL LES tool and an aeroelastic solver is described in Chapter 3. Furthermore, the grid sensitivity study discussed in Chapter 4 provides insight into the LES requirements for load calculations that might aid the future development of standard guidelines and procedures.

4. **Targeting specific wind conditions**: one of the great advantages of synthetic turbulence generators is their flexibility to target specific wind conditions, which allows prescribing the desired mean wind speed, TI, and shear exponent. Unfortunately, this is currently very hard to reach with LES because of the strong physical interdependency among the quantities [32]. If the use of LES-generated inflow is proven beneficial for load calculations, tackling this challenge would become important as an easy targeting specific conditions is essential for DLC calculations, where simulations need to be run for the whole operating range of the turbine. This aspect is not addressed in the present work and it is left for future research.

2   Introduction to GRASP and inflow validation

This chapter evaluates the ability of GRASP to capture realistic atmospheric flow conditions, mainly turbulence. GRASP, GPU-Resident Atmospheric Simulation Platform is a Whiffle's LES solver, which originates from the Dutch Atmospheric Large Eddy Simulation (DALES) model [33]. Unlike other LES codes, GRASP overcomes the barrier of large computational cost and LES operation in weather forecasting using the massive computer power offered by the GPUs. This parallel processing allows it to complete simulations 40 times faster than the traditionally used LES codes [34]. See Ciaran Gilbert et al. [35] for more information on the GRASP performance and an offshore wind farm case study.

This work aims to extend the advantages offered by GRASP to the wind industry by coupling it with OpenFAST. This coupling requires ASPIRE (Atmospheric Simulation Platform for Innovation Research and Education) as an interface (see Chapter 3). In other words, GRASP provides inflow parameters to OpenFAST, i.e. wind speed time histories to calculate the aeroelastic loads on a wind turbine.

Therefore, as a first step, the inflow parameters of GRASP are validated against measurements. The validation is carried out for three geographically different sites: a flat farmland, Cabauw; an offshore site, met mast IJmuiden; and a site with complex terrain, Rodeser Berg. The comparative analysis of horizontal wind speed, standard deviation, and turbulence intensity data of GRASP against the 10-min observational datasets is presented. These three sites use the standard hindcasting setup of GRASP, which takes boundary conditions like geostrophic parameters from ERA5 [36], surface roughness quantities from Corine, and terrain information from Actueel Hoogtebestand Nederland (AHN).

Furthermore, this validation study includes the influence of current developments in the LES code of GRASP, which consists of two parts: 1) an introduction of a stability-dependent correction factor ($f(Ri)$) to the sub-grid scheme (SGS), and 2) the re-calibration of the prefactor value (similar to the Smagorinsky constant) in the SGS. The GRASP SGS modelling is based on a K-diffusion approach and the value of K parameter is updated in the following two steps:

$$K_m = (c_s \Delta)^2 \sqrt{2S_{ij}S_{ij}} \tag{2.1}$$

$$K_m = \bar{K}_m f(Ri) \tag{2.2}$$

where,
K_m = local eddy viscosity,
c_s = dimensionless prefactor used in the subgrid models,
Δ = length scale in subgrid models,
S_{ij} = symmetric version of velocity gradient tensor,
Ri = Richardson number Both modifications impact the activity of the sub-grid scheme and aim to improve the representation of turbulence.

In the end, an academic case replicating an LES setup described in the literature is also presented for the Østerlid site [37]. A first comparison of the inflow quantities is carried out for this site introducing the setup used in the grid sensitivity study of Chapter 4.

2.1 Cabauw - a flat land

The Cabauw Experimental Site for Atmospheric Research (CESAR) provides high-quality atmospheric measurements from a 213 m meteorological mast [38]. This met mast is located on a open and flat landscape in the Netherlands with a mean elevation of 0.7 m below sea level. The aerial view of this site is shown in Figure 1(a), where the red marker denotes the met mast location. To validate the turbulence level, 10-min average horizontal wind speed and standard deviation data are analysed.

2.1.1 GRASP setup

Three different simulations were carried out to analyse the influence of the updated sub-grid scheme in turbulence prediction. The first simulation is a currently operational GRASP version, $GRASP_{NSC}$ based on subgrid scheme Rozema. The second simulation includes the aforementioned update in the sub-grid scheme of GRASP, i.e. introducing stability parameter and re-calibration of c_s (subgrid scheme Sullivan). In addition to the update, the third simulation has a lower surface roughness length $GRASP_{lowz0}$. Here, the surface roughness of uniform land use vegetation type is changed to 10 cm (from the original 25 cm) to analyse its influence on turbulence.

(a) Ground view   **(b)** Height Map
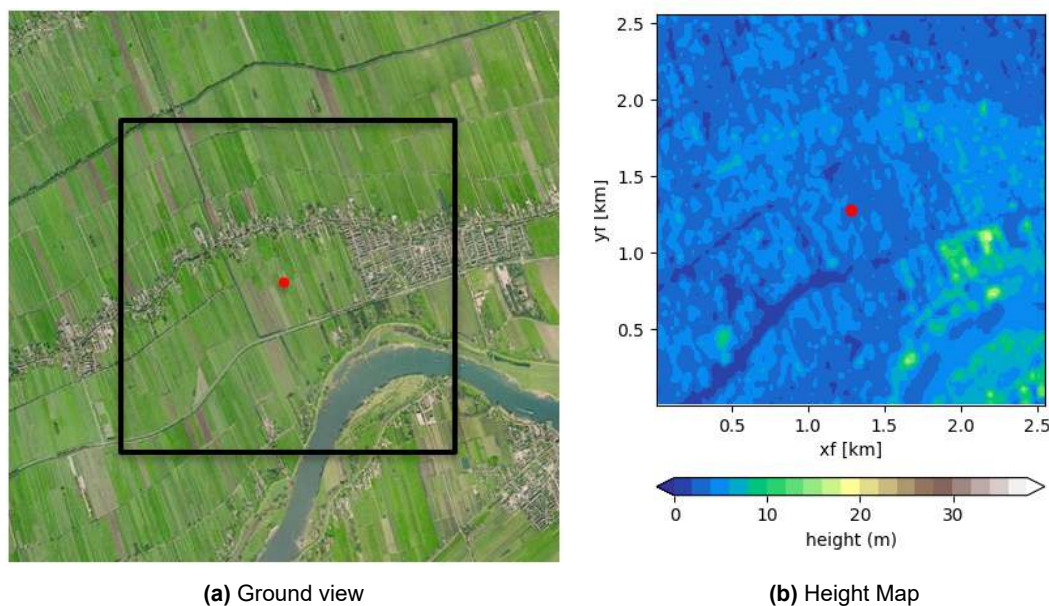
Figure 1: Illustration of the simulation domain used in GRASP for the Cabauw site: (a) ground view; (b) height Map. The met mast location is indicated by the red marker at the center of the domain. The black box (a) highlights the selected domain area of 2.5 x 2.5 km^2

(a) January 13, 2017   **(b)** February 2, 2017
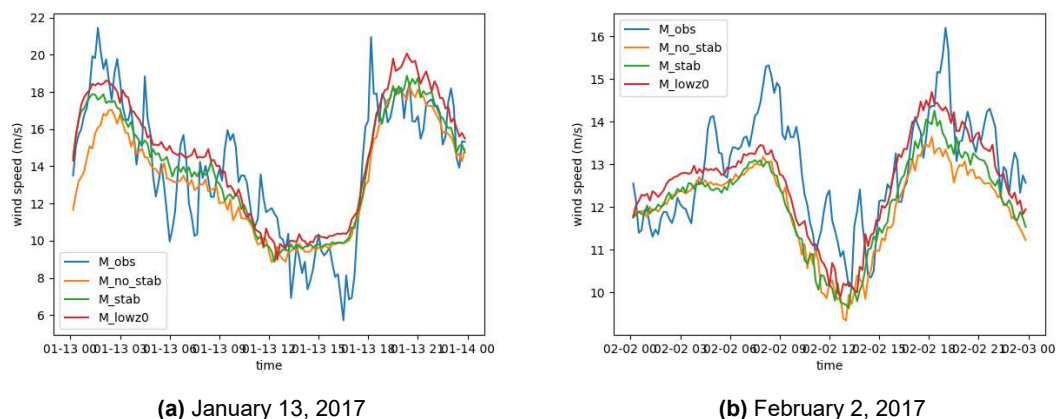
Figure 2: Cabauw site. Wind speed time series of observations and the three GRASP runs for two days of the year 2017, at 200 m altitude. In the legend $M\_$ denotes the norm of the horizontal wind speed vector.

All GRASP simulations have the same domain size (highlighted by the black box in Figure 1(a)) of 2.5 km x 2.5 km x 2.5 km, with a grid resolution of 40 m x 40 m x 20 m. Figure 1(b) represents the height variation within the domain, confirming the flat terrain. The simulations are run for a 100-day cluster, which is representative of a range of wind speeds and wind directions observed in the year 2017. The GRASP output is available at 10-min interval to compare against 10-min measurements (for all three sites).

2.1.2   Results

As a preliminary check, the wind speed time series of all simulations are compared with measurements. A brief overview of a two-day representative time series at 200m height is shown in Figure 2. In general, GRASP follows the observed wind speed trends, but has smaller fluctuations. The time series of the updated simulation, $GRASP_{SC}$ do not show significant difference as compared to the $GRASP_{NSC}$. In contrast, as expected, lowering the surface roughness value ($GRASP_{lowz0}$) increases the wind speed.

For a quantitative assessment of the performance, the density scatter plots of the horizontal wind speed at 80m height are examined. In Figure 3, error metrics of each simulation are summarised in the inset of each plot. It includes bias, Root Mean Square Error (RMSE), Root Mean Square Deviation (RMSD), normalized Mean Absolute Error (nMAE), and Pearson's correlation coefficient (ρ) between them. The colour map on the right-hand side of each figure indicates the population density.

Overall, the simulations show low bias (<0.4 m/s), good correlation (>0.94), and low RMSE (<1.5 m/s) values confirming the good performance of GRASP in capturing horizontal wind speed. Similar to the wind speed time series (Figure 2), $GRASP_{NSC}$ under-predicts the wind speed with a bias of 0.1 m/s. The update in the sub-grid scheme ($GRASP_{SC}$) reduces this bias to 0.04 m/s (Figure 3(b)). On the other hand, lowering surface roughness ($GRASP_{lowz0}$) leads to an over-prediction of the wind speed of 0.33 m/s.

In the next step, the simulated 10-min horizontal wind speed standard deviation (σ_m) values are

(a) $GRASP_{NSC}$ **(b)** $GRASP_{SC}$ **(c)** $GRASP_{lowz0}$
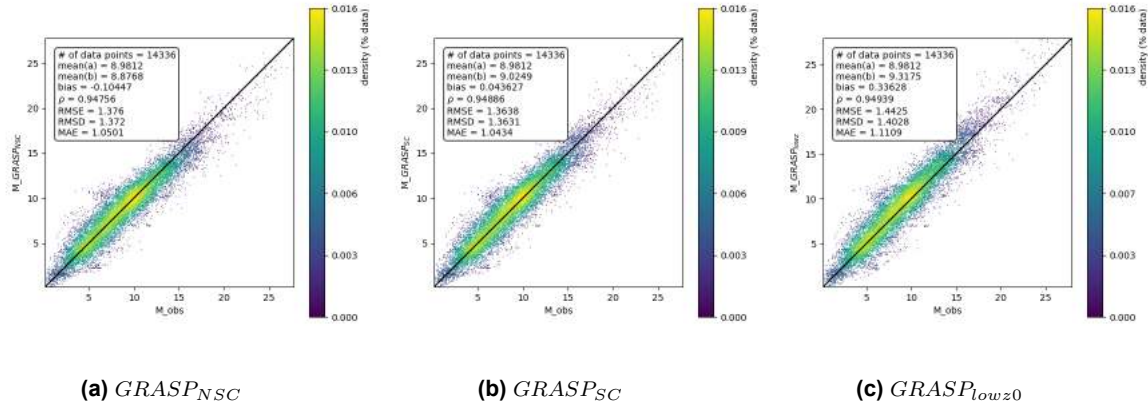
Figure 3: Cabauw site. Comparison of horizontal wind speed observations against (a) $GRASP_{NSC}$, (b) $GRASP_{SC}$, and (c) $GRASP_{lowz0}$, at a height of 80 m using density scatter plots. The associated error metrics are summarised in the inset of each plot.

compared against observations. Figure 4 represents the variation in σ_m with wind speed using density scatter plots for all simulations, at 80 m height. As visualized, σ_m from the simulations are clustered in a small region, showing a fairly linear correlation with wind speed, whereas observations are comparatively scattered (Figure 4(a)). In $GRASP_{NSC}$, two separate clusters of σ_m are observed (Figure 4(b)). This separation reduces with the updated sub-grid scheme (Figure 4(c) & (d)).

The average σ_m per wind speed bin shows a similar increasing trend for all simulations and observations. Figure 5 summarises the average σ_m variation at different heights. The simulations over-predict the standard deviation, and this over-prediction margin decreases as the altitude increases. It can be said that surface roughness has a significant impact on the standard deviation compared to the update in the sub-grid scheme. $GRASP_{lowz0}$ (in blue) follows observations (in black) closely compared to the other simulations. At higher altitudes, however, the simulations slightly under-predict σ_m.

The horizontal turbulence intensity (TI) is defined as,

$$\text{TI} = \frac{\sigma_M}{M} \tag{2.3}$$

where TI denotes horizontal turbulence intensity, M is the 10-min average horizontal wind speed and σ_m is a 10-min standard deviation of horizontal wind speed.

Figure 6 illustrates the TI curve for wind speed higher than 3m/s for all channels at different heights; 20 m, 80 m, and 200 m. The results are in line with the standard deviations; i.e. simulations over-predict TI values at lower heights. Higher up, at 200 m, all simulations show a slight underestimation. The simulation with lowered surface roughness ($GRASP_{lowz0}$) follows the observed TI curve more closely, highlighting the impact of surface roughness on turbulence.

(a) Observations

(b) $GRASP_{NSC}$

(c) $GRASP_{SC}$

(d) $GRASP_{lowz0}$
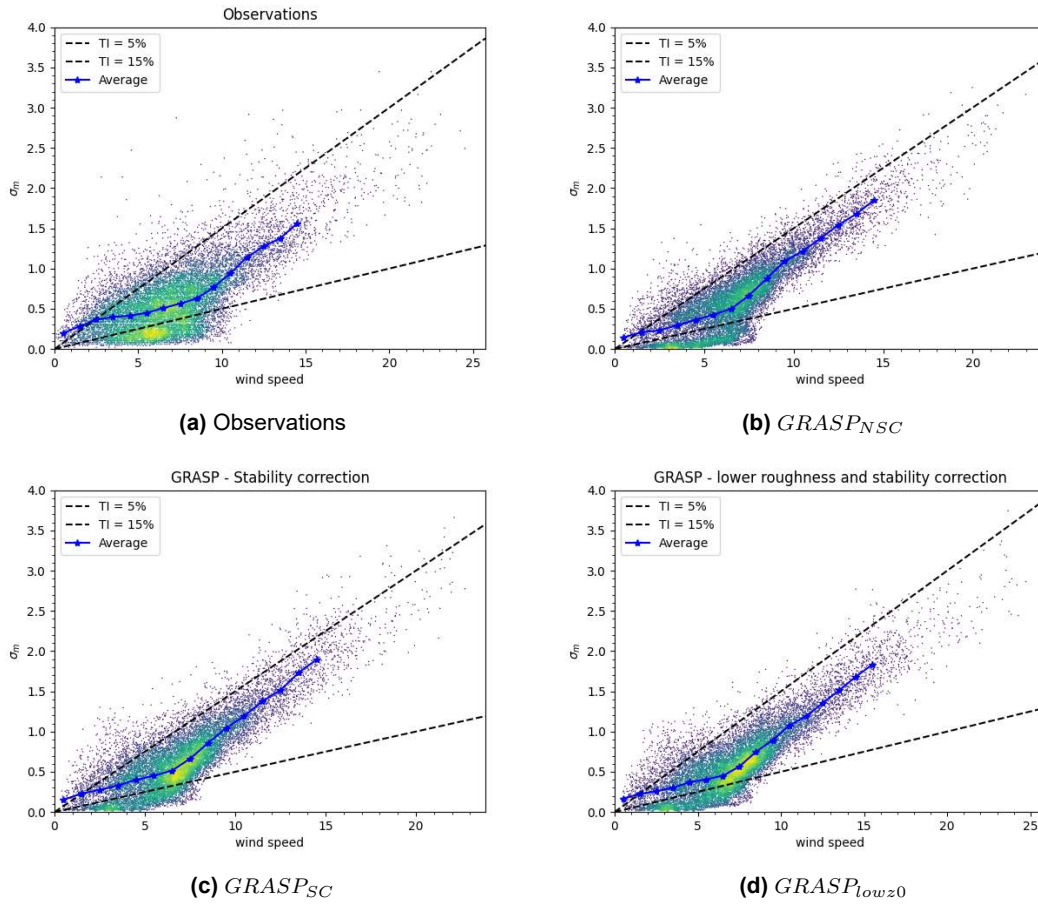
Figure 4: Cabauw site. Density scatter plot of 10-min horizontal wind speed standard deviation w.r.t. 10-min average wind speed at 80 m height. Averages of these standard deviations per wind speed bin are shown by the blue curve. The two black lines represent slopes of 5 and 15 %, i.e. TI.

(a) at 20 m

(b) at 80 m

(c) at 200 m
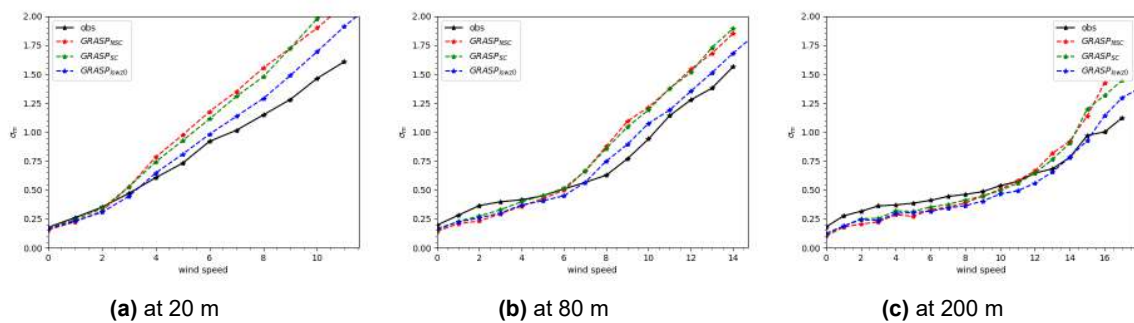
Figure 5: Cabauw site. Comparison between average observed (in black) and GRASP standard deviations per wind speed bin at different heights.

(a) at 20 m   **(b)** at 80 m   **(c)** at 200 m
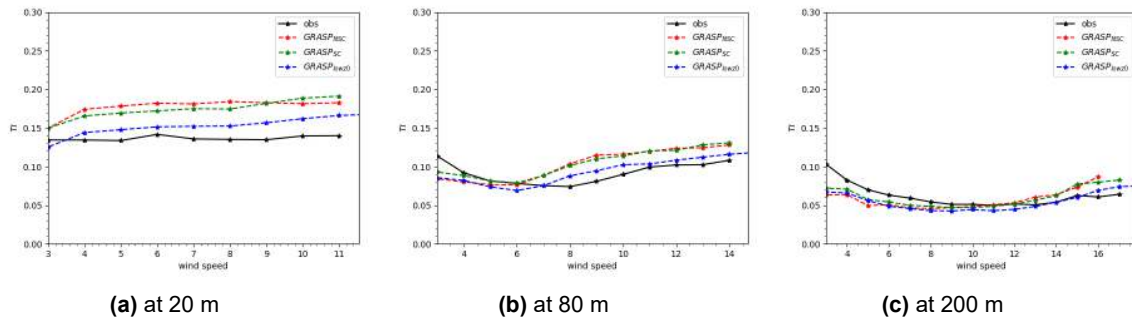
Figure 6: Cabauw site. Comparison between observed (in black) and GRASP average turbulence intensities per wind speed bin

(a) at 20 m   **(b)** at 80 m   **(c)** at 200 m
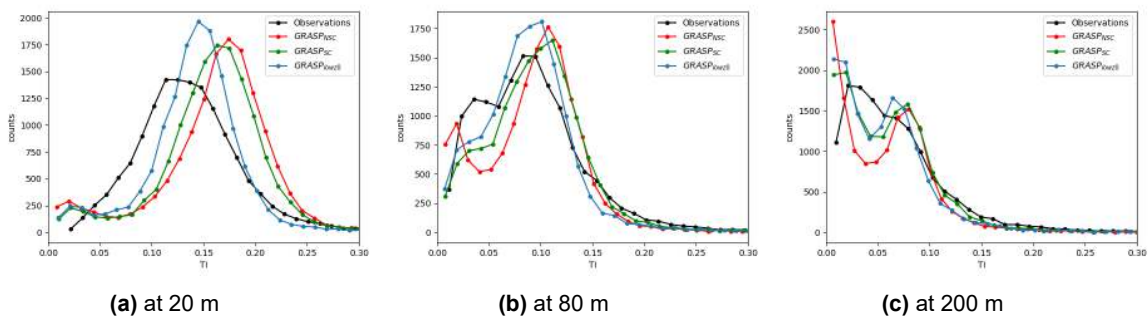
Figure 7: Cabauw site. Comparison of turbulence intensity distribution between observations and GRASP simulations at three heights. The effect of stability correction is most evident at height 80 m (b).

The precise distribution of TI is one of the critical factors in wind turbine design. Thus, Figure 7 presents histograms of TI distribution at the three different heights. The significant impact of the updated sub-grid scheme can be observed in these figures. $GRASP_{NSC}$ has a TI distribution concentrated at higher TI values compared to the observations. At increasing heights, it shows two distinct peaks which are not seen in the measurements. At 80 m (Figure 7(b)), these peaks are adjusted by the updated sub-grid scheme, highlighting its effect on the distribution of TI. However, at 200 m height (Figure 7(c)), these peaks are present even after the update in GRASP, though with reduced intensity compared to the $GRASP_{NSC}$.

2.2   IJmuiden - an offshore site

The IJmuiden meteorological mast is located in the North Sea, 75 km west of IJmuiden, a coastal city in the Netherlands. Wind measurements from cup anemometers mounted at 27m, 58.5m, 85m, and 92m height are available. The measurement campaign was subject to strict quality control and the wind measurements from the highest anemometer (92m) were cross-validated with a ground-based Lidar in previous work [39]. For this site, two GRASP simulations were performed - one with the operational GRASP version ($GRASP_{NSC}$) and the second with the updated GRASP version ($GRASP_{SC}$) as for Cabauw. The domain size and grid resolution of these simulations are the same, i.e., 2.5 km x 2.5 km x 2.5 km and 40 m x 40 m x 20 m, respectively. These simulations are also carried out for 100 days, representing a range of wind

(a) $GRASP_{NSC}$ **(b)** $GRASP_{SC}$
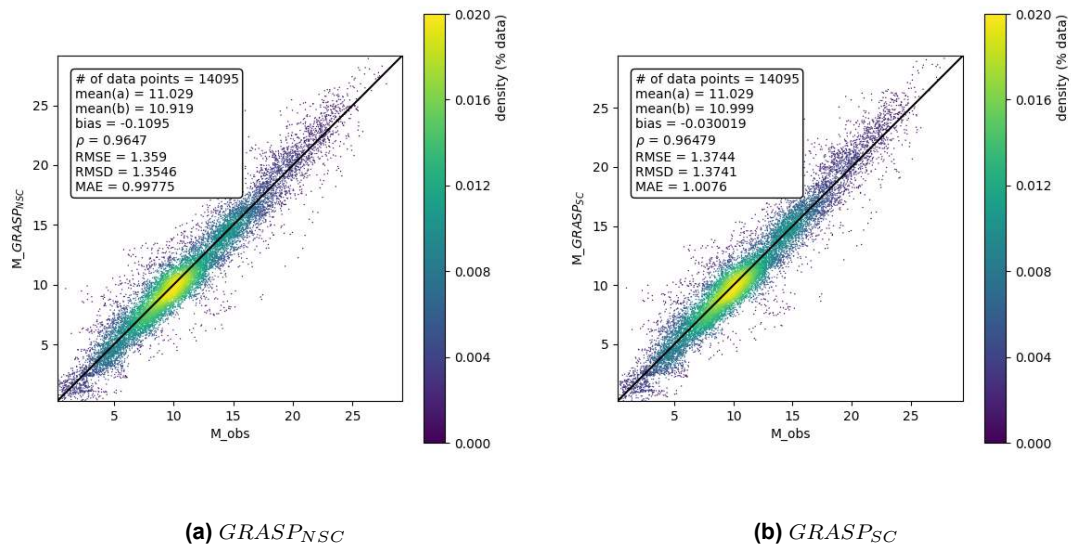
Figure 8: IJmuiden site. Comparison of horizontal wind speed observations with (a) $GRASP_{NSC}$ and (b) $GRASP_{SC}$, at the height of 92 m, using density scatter plots. The associated error metrics are summarised in the upper left box of each plot.

speeds and wind directions of the year 2015.

2.2.1   Results

Figure 8 compares the horizontal wind speed of the simulations with observations at 92m height using density scatter plots. The error metrics are presented in the inset of each figure. Both simulations show a very high Pearson's correlation coefficient of 0.96. This brings confidence on GRASP's ability of accurately capturing wind speeds at an offshore site. With the updated GRASP version, the bias in wind speed drops to 0.03 m/s from 0.11 m/s ($GRASP_{NSC}$). However, other error scores are similar in magnitude for both simulations.

In Figure 9, the density scatter plots of σ_m values show an increasing trend with wind speed for the observations and the simulations at 92 m height. The average standard deviation values per wind speed bin are similar for both simulations ($GRASP_{NSC}$ and $GRASP_{SC}$ in Figure 10). In comparison to the measured σ_m, the simulations show a slight over-prediction at 27 m height (Figure 10(a)), and the error reduces with increasing altitude. However, simulations under-predict the average σ_m for the lower wind speed bins. The range of wind speed bins for the under-prediction in σ_m increases with height (from 3 m/s to 12.5 m/s).

Turbulence intensity curves (Figure 11) show similar behaviour as the standard deviations, confirming the larger impact of σ_m over wind speed. In summary, the simulations slightly over-predict TI at 27 m height and follows precisely afterwards, except under-prediction at lower wind speed bins.

The similarity in the simulations is also visualised in the histograms of TI distribution (Figure 12). At 27 m altitude (Figure 12(a)), both simulations show peaks at higher TI values than obser-

(a) Observations **(b)** $GRASP_{NSC}$ **(c)** $GRASP_{SC}$
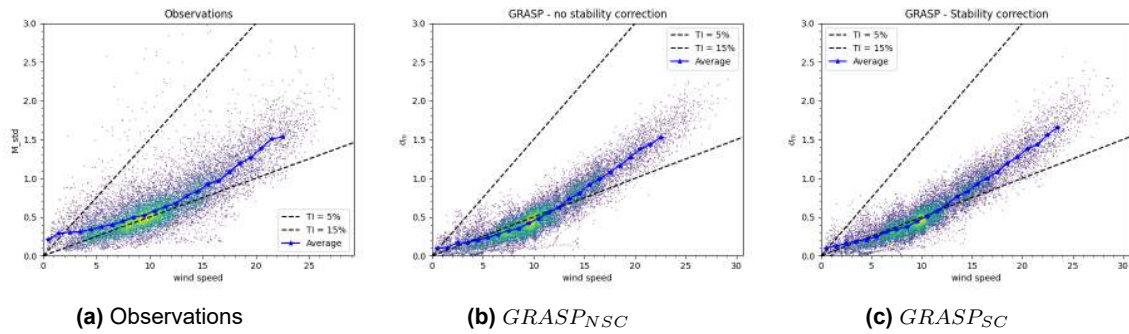
Figure 9: IJmuiden site. Density scatter plot of 10-min horizontal wind speed standard deviation w.r.t. 10-min average wind speed at the height of 92 m. Average of these standard deviations per wind speed bin are shown by blue curve. The two black lines represent slopes of 5 and 15 %, i.e. TI.

(a) at 27 m **(b)** at 58 m **(c)** at 92 m
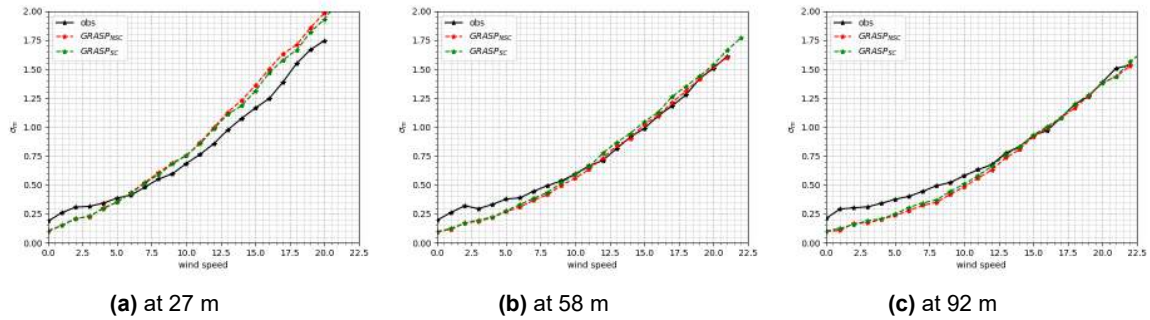
Figure 10: IJmuiden site. Comparison between average observed (in black) and GRASP standard deviations per wind speed bin at different heights.

(a) at 27 m **(b)** at 58 m **(c)** at 92 m
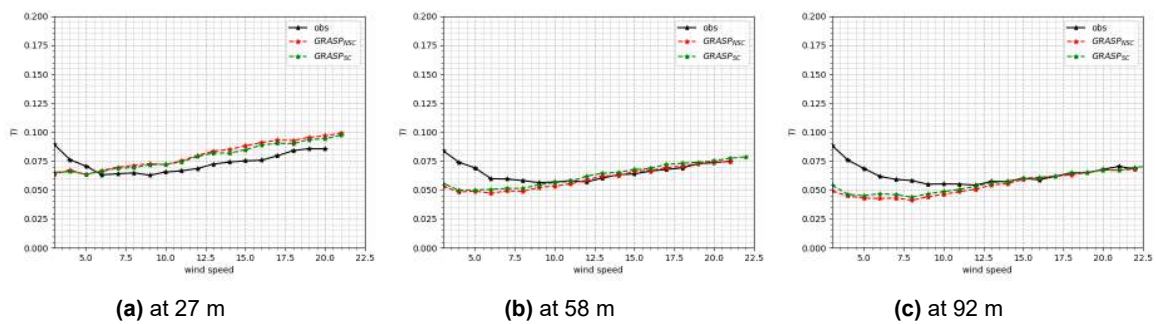
Figure 11: IJmuiden site. Comparison between observed (in black) and GRASP average turbulence intensities per wind speed bin.

| **(a)** at 27 m | **(b)** at 58 m | **(c)** at 92 m |
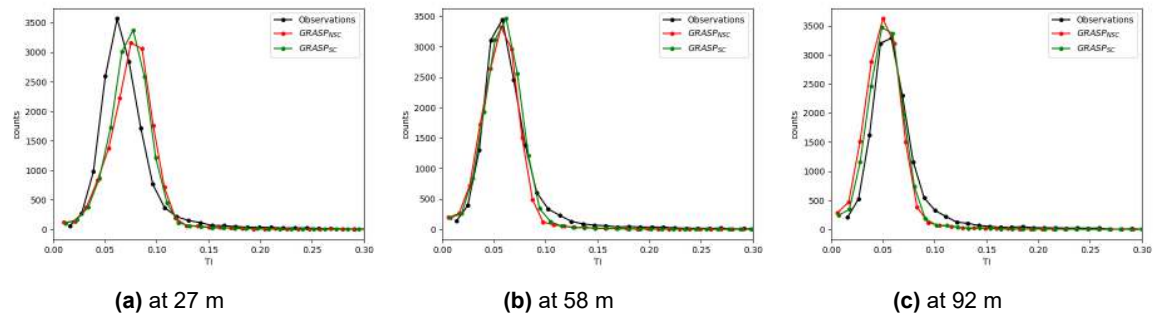
Figure 12: IJmuiden site. Histograms to compare the turbulence intensity distribution between observations and GRASP simulations at three heights. The effect of stability correction is most evident at height 92m (b).

vations (in black). This difference is reduced as the height increases, and the simulations show an excellent agreement with the measurements. In conclusion, GRASP captures the offshore turbulence precisely, and the updated sub-grid scheme does not influence turbulence at IJmuiden. One possible reason for this can be the higher instability observed at offshore sites caused by the lack of diurnal cycles, smaller changes in the wind speed and the heat flux with height [40].

## 2.3 Rodeser Berg - a site with complex terrain

This section covers the turbulence validation of a complex onshore site, Rodeser Berg, which is a part of a ridge of hills in Germany. This site is surrounded by a forest area and has the highest point 417 m above sea level. The high-quality weather data of the site is available from a 200 m tall met mast located at the southwestern edge of the hill (see Figure 13(a)). To incorporate the effect of a varying orography, the selected domain size is significantly larger than the aforementioned sites, i.e. 10.2 x 10.2 km^2 (Figure 13(b)).

One year simulation from May 2013 to 2014 is performed with the operational GRASP version $GRASP_{NSC}$. The domain size and grid resolution of the simulation is 10.2 km x 10.2 km x 2.5 km and 80 m x 80 m x 20 m, respectively. The impact of the updated GRASP version on this site will be investigated in a future research.

2.3.1 Results

Figure 14 represents the density scatter plot of horizontal wind speed at heights 40 m, 80 m and 140 m. The performance of GRASP w.r.t. observations is summarised using error metrics, which are shown in the inset of the respective figures. In general, GRASP over-predicts wind speed, and this over-prediction decreases with an increase in height (from a bias of 0.6 m/s to 0.3 m/s). Similarly, the correlation between simulated and observed wind speeds increases with height (from 0.8 to 0.9). However, errors are slightly higher for this site compared to the aforementioned sites most likely as a result of the complex terrain characteristics.

Figure 15 illustrates the variation in standard deviation with wind speed for the simulation and observations at 140 m altitude. Observations are scattered over the range of σ_m and wind

(a) Ground view   **(b)** Height Map
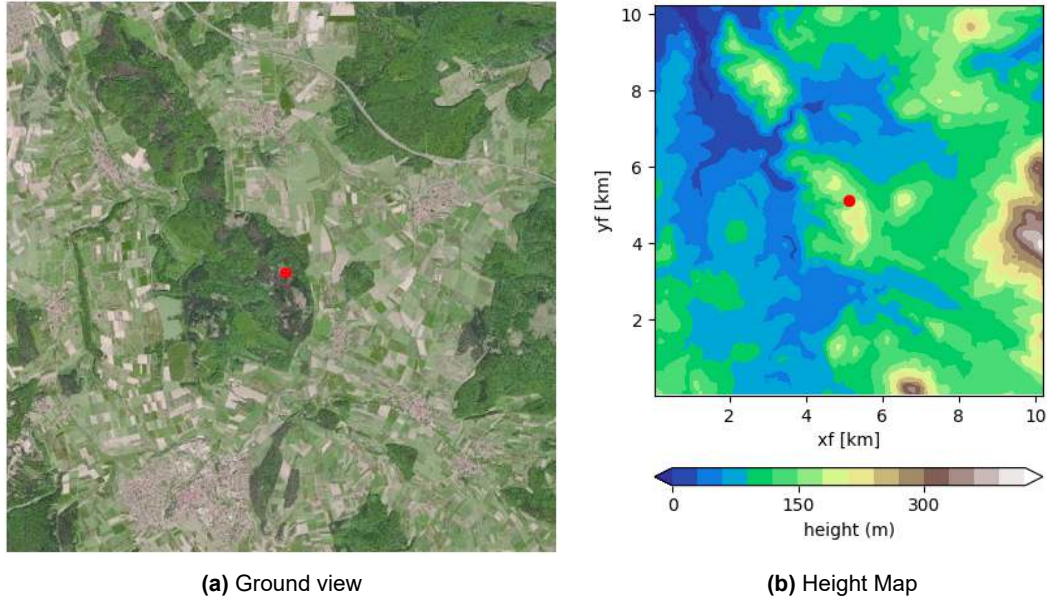
Figure 13: Rodeser Berg site. Illustration of the GRASP simulation domain: (a) ground view (10.2 x 10.2 km^2); (b) height map. The location of the met mast is denoted by the red marker at the center of the domain.

(a) at 40 m   **(b)** at 80 m   **(c)** at 140 m
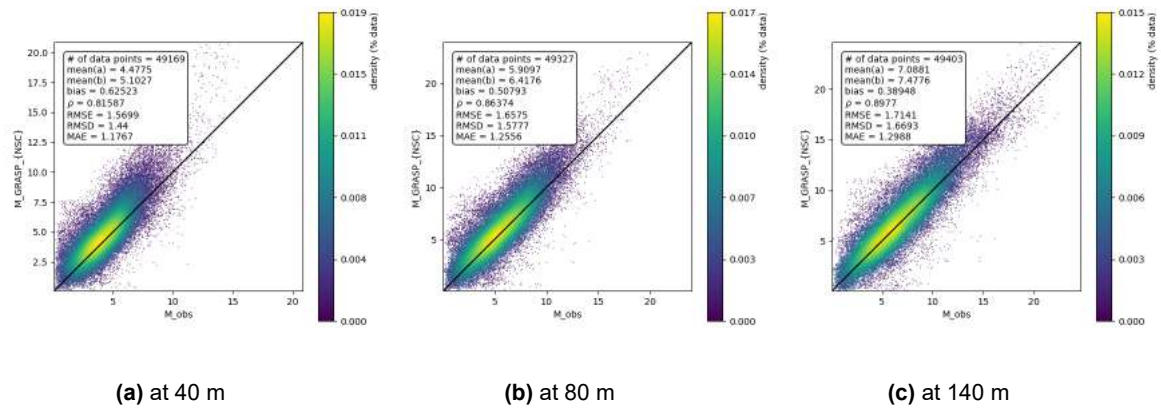
Figure 14: Rodeser Berg site. Comparison between observed (in black) and GRASP average turbulence intensities per wind speed bin.

(a) Observations **(b)** $GRASP_{NSC}$
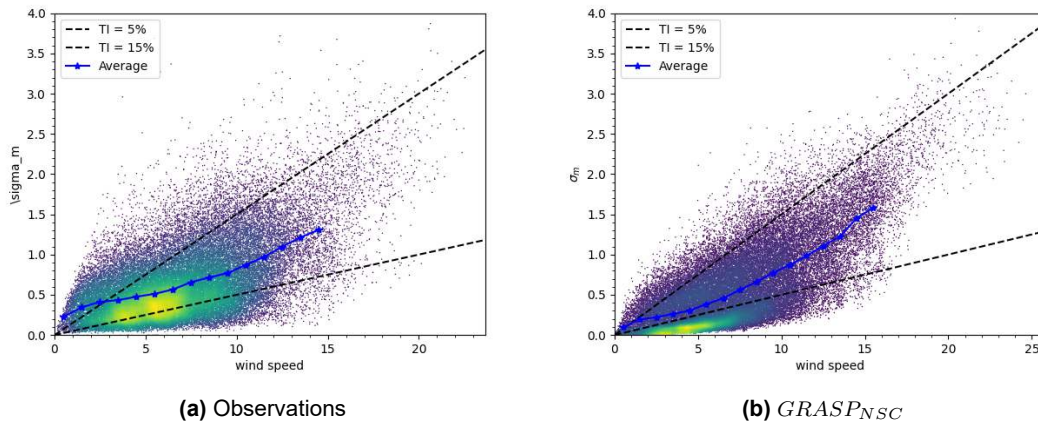
Figure 15: Rodeser Berg site. Density scatter plot of 10-min horizontal wind speed standard deviation w.r.t. 10-min average wind speed at 140 m height. The average standard deviation per wind speed bin are shown by the blue curve. The two black lines represent slopes of 5 and 15 %, i.e. TI.

(a) at 40 m **(b)** at 80 m **(c)** at 140 m
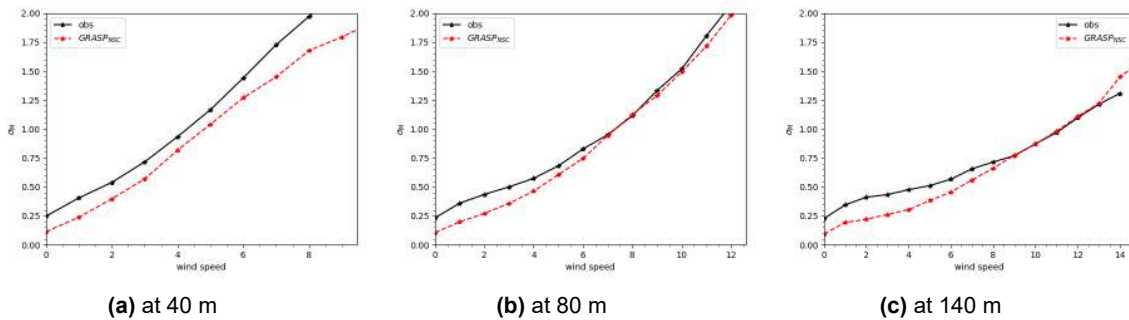
Figure 16: Rodeser Berg site. Comparison between observed (in black) and GRASP average standard deviation per wind speed bin.

speeds (Figure 15(a)). On the other hand, σ_m from the simulation are concentrated for lower standard deviation values (yellow region is below 0.2 in the Figure 15(b)).

The average σ_m values per wind speed bin are higher for observations compared to the simulation. With the increase in height, the discrepancies in average standard deviations reduce for higher wind speed bins.

Figure 17 represents the average TI variation per wind speed bin for simulations and observations. It follows a similar trend as the standard deviation curves (Figure 17). At 40 m altitude, the average turbulence intensities (in red) from the simulation are lower than the observations (in black). With the increase in height, the discrepancies between TI values reduce for higher wind speeds. GRASP turbulence intensities are under-predicted for lower wind speeds.

The turbulence intensity distribution of Rodeser Berg (Figure 18) shows similar behaviour as Cabauw, for $GRASP_{NSC}$ (Figure 7). At 40 m height (Figure 18(a)), GRASP under-predicts the turbulence intensities with the peak shifted to lower TI values. With an increase in height, two

| (a) at 40 m | (b) at 80 m | (c) at 140 m |
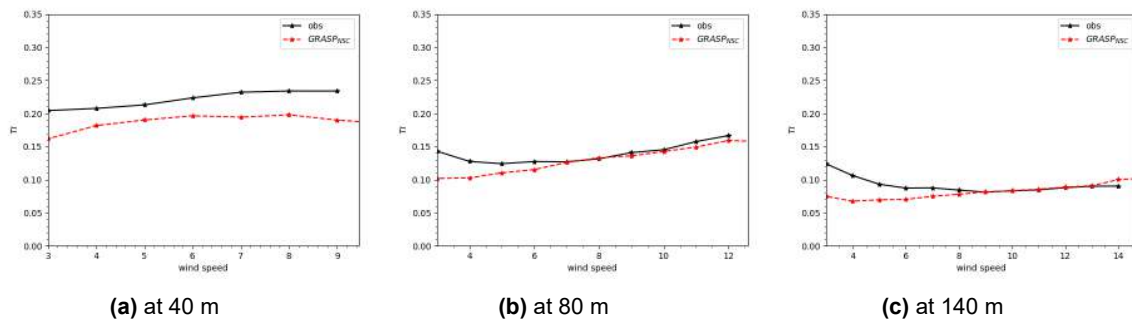
Figure 17: Rodeser Berg site. Comparison between observed (in black) and GRASP average turbulence intensities per wind speed bin.

| (a) at 40 m | (b) at 80 m | (c) at 140 m |
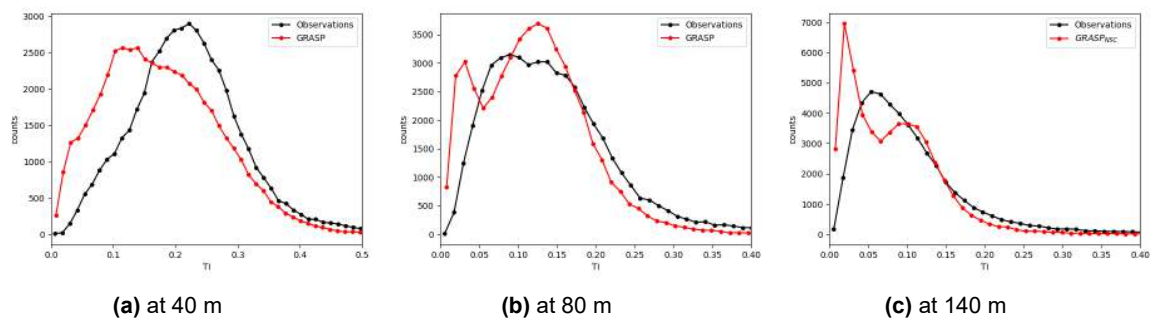
Figure 18: Rodeser Berg site. Histograms comparing the turbulence intensity distribution between observations and GRASP simulations at three heights. The effect of stability correction is most evident at 80 m height (b).

distinct peaks in the TI are visible. Therefore, based on the results of Cabauw Figure 7, the sub-grid scheme update of GRASP is expected to improve the agreement between measurements and simulations. and its verification for the Rodeser Berg site is recommended for future work.

2.4   Discussion

A comparative analysis of LES simulations and observations has been presented for the three sites, Cabauw, IJmuiden, and Rodeser Berg. These sites are good representatives of geographic variations with the availability of high-quality measurements. For all sites, GRASP showed good agreement with the 10-min average wind speed observations. The performance score was found to be higher for the offshore site (IJmuiden) compared to the onshore ones. This can be related to the available surface roughness data and the limitation of grid resolution for defining obstacles. For all three sites, GRASP under-predicts TI at lower wind speeds, but precise agreement is observed near normal operational wind speed of a wind turbine.

The introduction of a stability parameter and re-calibration of c_S have significantly reduced the bias in wind speed. Even though the TI curves were similar to the current GRASP version ($GRASP_{NSC}$), the update is promising for correcting the abnormal peaks found in the TI distribution of $GRASP_{NSC}$. Also, the updated TI distribution showed higher density for low TI values, which is inline with observations. On the other hand, lowering the surface roughness

value (in addition to the update in sub-grid scheme) led to a higher bias in wind speed but lower discrepancies with the TI curves. It is expected that by combining the introduction of stability parameters in the SGS model with more accurate surface roughness data would significantly improve the turbulence energy distribution for onshore sites.

2.5 Recommendations for future work

Based on the results of Cabauw (section 2.1), it is recommended to test the updated GRASP version for the Rodeser Berg site and assess the influence on the turbulence intensity distribution. Also, the scope of the proposed analysis can be extended to validate the turbulent kinetic energy of these sites by looking at energy spectra. This would help analysing the energy distribution over different spatial and temporal scales and highlighting any missing scales.

2.6 Østerlid cases

As a first step towards the detailed grid sensitivity study presented in Chapter 4, a few ABL properties obtained with GRASP have been compared to publicly available results obtained by Peña et al. [26] with the Weather Resource Forecasting model (WRF [41]), as well as met mast measurements from the Østerlid site in Denmark.

Østerlid is an onshore site where high-quality measurements from a 250 m met mast are available and the atmospheric turbulence, for a wide range of wind directions, was found to be close to homogeneous thanks to the wide undisturbed sector and the flat terrain surrounding the site [37]. The long measurement campaign allowed filtering of the data for different ABL stability conditions, which were used to validate LES results from WRF [26].

The GRASP simulations discussed in this section use similar input quantities as those used in WRF, with both initial and boundary conditions (including geostrophic forcing, terrain properties, and surface fluxes) following the setup described in [26]. A simulation domain of 1024 m x 1024 m x 2048 m has been used with a rectangular grid of 32 equal elements (32 m long) in longitudinal and lateral directions, and 128 in the vertical direction gradually stretched from an 8 m length at the lowest level up to 28 m at the top of the domain. A dynamic time step selection method based on a maximum instantaneous Courant number of 1 has been adopted in all simulations, corresponding to an average time step size of approximately 2 s (slightly different for each stability condition). The governing equations have been solved explicitly with a third-order Runge-Kutta scheme for the time discretization, and second-order schemes for all convective terms. Finally, the Rozema model [42] has been used for the sub-grid scales with the default filter size being the geometric average of the cell dimensions.

The potential temperature (θ) and mean horizontal wind speed (M) profiles for the first hour as well as a selected simulation hour (as defined in [26]) are reported in fig. 19 for heights up to 500m. Very good agreement is always found for the first simulated hour due to the matching initial conditions. For the later hours, the neutral ABL case (fig. 19a) shows the best agreement with respect to the WRF results for both wind speed and potential temperature. Larger differences are found in the unstable case (fig. 19b), where potential temperature profiles are very similar because of the same prescribed heat flux, but the GRASP simulations find a lower mean wind speed in the surface layer. In the stable case (fig. 19c), discrepancies in the potential temperature profile above 300 m height yield slightly different velocity profiles with a supergeostrophic peak shifted towards higher altitudes than WRF. The differences between
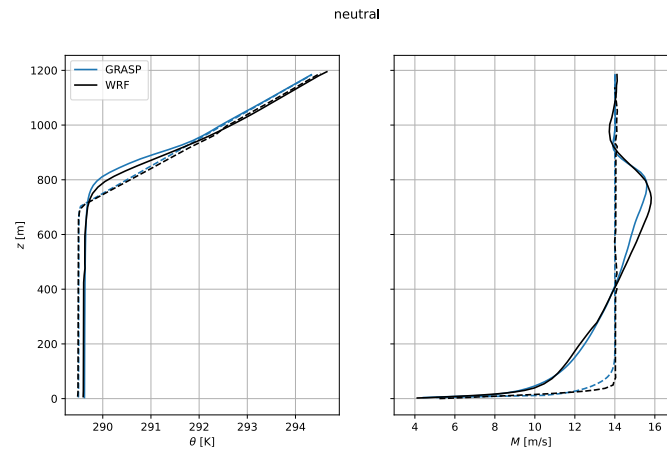
**(a)** Neutral
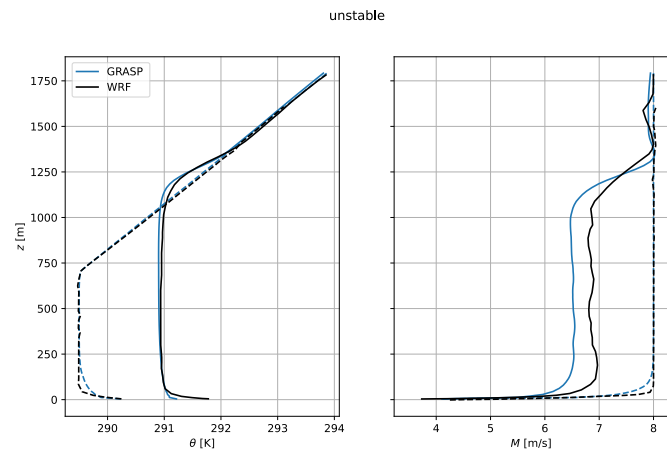
(b) Unstable
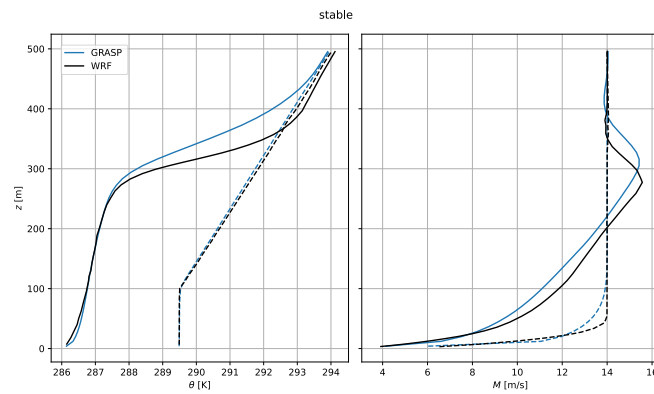
(c) Stable

Figure 19: Østerlid site. Vertical profiles of potential temperature and horizontal wind speed magnitude for the different stability conditions from GRASP and WRF simulations (from Peña et al. [26]). The dashed lines show the average values for the first simulated hour, whereas the solid lines refer to the selected hours defined in [26].

GRASP and WRF observed in the stable and unstable cases are not surprising due to the sensitivity of inflow profiles on grid resolutions, SGS models, and discretization schemes, especially when buoyancy effects are not negligible.

Figure 20 shows the comparison of wind speed profiles normalized by the friction velocity (u^*) for the different stability conditions including simulated and measured values from Peña et al. [26] as well as GRASP results. The large variance in the measurements and the fact that these are limited by the height of the met mast (where simulations model the full ABL height) hinders the quantitative validation of numerical results. A very good agreement is found for the neutral case (fig. 19a), whereas the stable and neutral cases show larger differences, with the GRASP results being a bit farther from the mean measured profiles than WRF, although still within the uncertainty band of the measurements. Here it is noted that, besides the already mentioned sensitivity to numerical model settings, the agreement between measurements and simulations is also dependent on the simulation interval selected for the analysis. The agreement between GRASP and observations is likely to improve if a different hour than the one proposed in [26] is selected.

Despite the difficulties in performing a quantitative validation of the results for all stability conditions, the quasi-canonical flow at Østerlid combined with the detailed description of a LES set up already publicly available have induced the authors to select this site to perform the grid sensitivity study presented in Chapter 4.

(a) Neutral
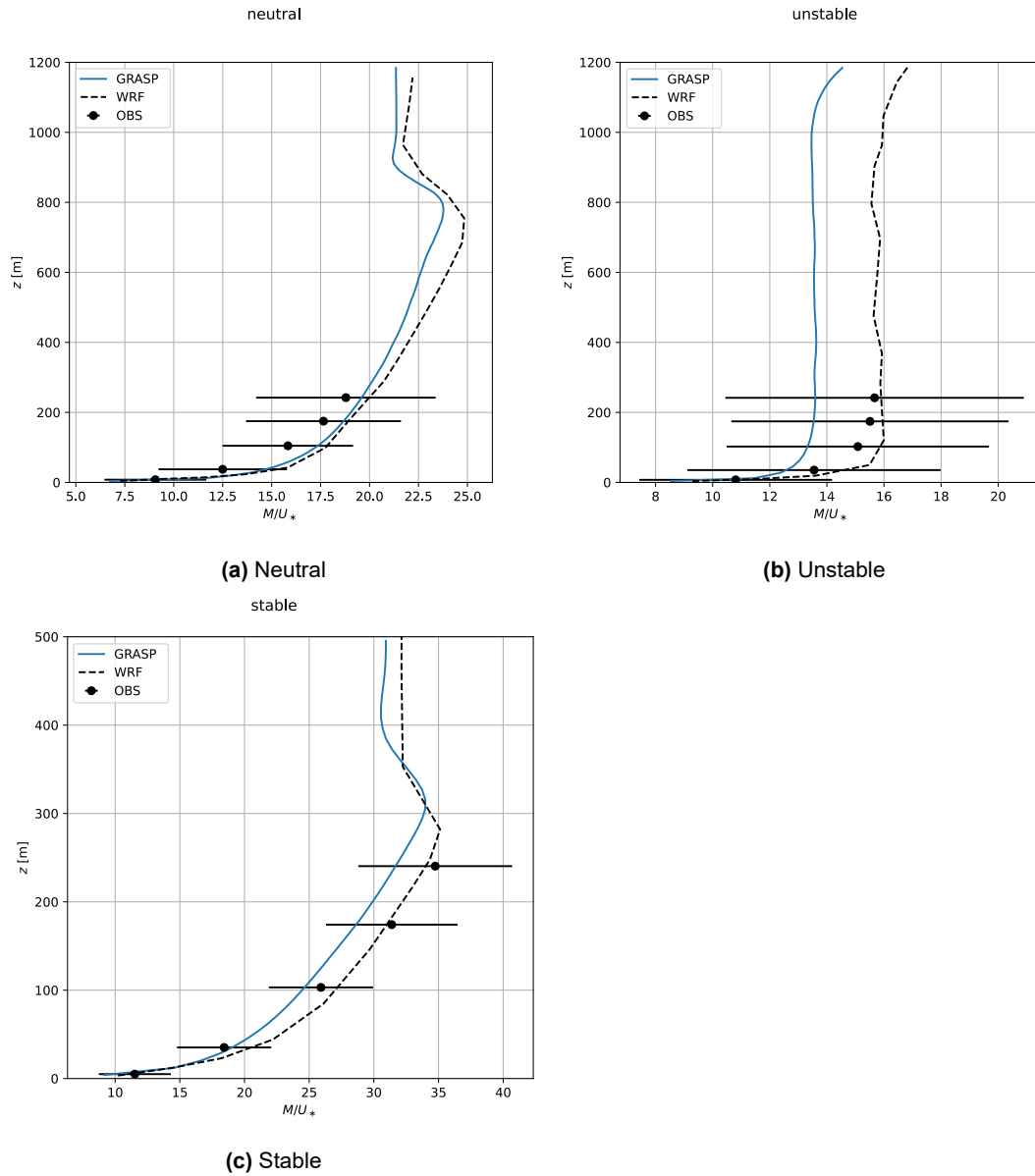
(b) Unstable

(c) Stable

Figure 20: Østerlid site. Normalized simulated and observed wind profiles for neutral (a), unstable (b), and stable (c) conditions. The error bars denote 1 standard deviation from the mean of the observations. Measurements and WRF results are taken from Peña et al. [26].

3 Coupling GRASP with a multi-physics wind turbine simulation tool

3.1 Introduction

Having compared GRASP-generated inflow quantities against observations from different sites, the next step is to enable the use of GRASP in the context of aeroelastic load calculations. For this reason, a coupling with OpenFAST [30] has been developed as described in this chapter.

Wind turbine models in computational fluid dynamics (CFD) can be classified into blade resolving models and actuator models. In blade resolving models, the computational grid conforms with a wind turbine surface and a no-slip boundary condition is enforced. However, the relevant flow length scales around the wind turbine and the atmospheric boundary layer differ significantly. Around the wind turbines, the required spatial resolutions are down to millimeters, while in atmospheric LES, the resolutions range from meters to hundreds of meters. The grid resolution affects both the evaluation time per time-step and the maximum time step size, which should respect the Courant–Friedrichs–Lewy (CFL) condition for stable simulations. Therefore, simulating several years or forecasting becomes infeasible with the blade resolving models, and faster models are required.

The actuator methods model the turbines with forcing terms that act on the cell volumes of the CFD grid. The actuator models induce the velocity at the turbine location, commonly modeled as infinitely thin discs (AD) or lines (AL). It takes the velocity field around the turbine as an input, and the point forces acting on the turbine are the output. With an AD approach, the aerodynamic forces are estimated from the turbine characteristic curves, whereas the AL method models the blades as lifting lines and relies on airfoil data to evaluate forces with the blade element theory [5].

Compared to AD, the AL model can predict asymmetric wakes with a helical shape and captures the tip and root vortices. However, the AL method is computationally more expensive than AD but still substantially cheaper than blade resolving methods. For AL models, an additional condition arises, which limits the maximum time step to the time the blade tip sweeps a cell. The tip speed for a large wind turbine is roughly one order of magnitude higher than the wind speed. Therefore, the allowed time step is one order of magnitude lower for AL than for AD.

3.2 The GRASP-OpenFAST coupling

To enable the use of ABL LES for wind turbine load calculations, GRASP has been coupled to OpenFAST [30], an open-source multi-physics wind turbine simulation tool from the US National Renewable Energy Laboratory (NREL) collecting several modules. As mentioned in the previous chapter, running on GPUs allows GRASP to simulate the ABL with LES at a lower computational cost than traditional software. Coupling GRASP with OpenFAST opens a wide range of modelling possibilities, providing a unique tool for aero-hydro-servo-elastic simulations of a wind turbine and its subsystems based on LES-generated inflow. Similar capabilities may be reached using the open-source SOWFA-OpenFAST coupling [29] as well, but losing the computational cost savings GRASP offers.

TNO PUBLIC

GRASP is a dynamic module that is executed through an C++ interface called ASPIRE. ASPIRE also provides an API for other modules. OpenFAST is coupled through its C++ interface to AS-PIRE as a dynamic plugin. When the plugin is activated by the user, the interface guarantees the correct information flow between ASPIRE and OpenFAST, which in turn transfers the information to its modules. Note that there is no restriction on which OpenFAST modules can be used in the coupled simulations other than the computational cost of adding complexity.

The ASPIRE plugin requires a separate input file to describe the turbine locations, interpolation function, projection function, path to OpenFAST turbine specification file, output writing options, etc. The timestep of OpenFAST should be the same or lower than the GRASP timestep. If a smaller timestep is used, OpenFAST is executed several times during each GRASP timestep.

The user must also specify whether a one-way or a two-way coupling is used. If a one-way coupling approach is selected, the turbine presence is neglected by the LES solver and standard wake models have to be used in the aerodynamic module to account for the rotor plane induction (the LES flow is undisturbed). Hence, the plugin only takes care of communicating the local wind velocity vector at each OpenFAST time step at each aerodynamic control point by interpolating the velocity field from the LES grid.

When the AL model is used, forcing terms acting on the cell volumes of the LES grid around blade and tower locations are introduced (as described in Section 3.1). These momentum sources replicate the local momentum exchange, disturbing the incoming flow (i.e. reproducing the induction field) and generating a wake. The main challenge of the AL coupling is modelling the point forces in the LES domain without affecting the convergence of the solver. A common approach, which is used by the plugin, is to project the point forces as body forces (f) to the nearby cells with a Gaussian function [8]:

$$f = \frac{F}{\epsilon^3 \pi^{3/2}} \exp(-[r/\epsilon]^2) \qquad (3.1)$$

where F is the point force, ϵ is the projection width, and r is the distance between the force point and the cell center. The projection width is a simulation-dependent parameter, which should be higher than two times the cell size to avoid numerical instabilities [43]. The higher the width, the farther the force smears and the lower the magnitude of f.

The coupling of GRASP with OpenFAST offers the possibility to use TNO's library of aerodynamic solvers (AeroModule [44]), hereinafter abbreviated as AM) as well by exploiting its existing interface with OpenFAST [45]. To allow the coupling with LES, a new AL solver has been developed as an alternative to the Blade Element Momentum (BEM) and free vortex wake solvers already in AM. Several BEM routines could be reused to develop the AL solver as the blade element theory is used by both. The AL does not need the momentum part, though, as the induction comes from the CFD, making it simpler than BEM. Being integrated in AM, the new solver takes advantage of the common airfoil aerodynamics, inflow treatment, and interpolation subroutines. A few new routines have been added to communicate the local wind vector (coming from the LES) at each control point at every time step.

A sketch of the coupling for a simple case using just ElastoDyn as the structural module and AM for the aerodynamic calculations is depicted in fig. 21.
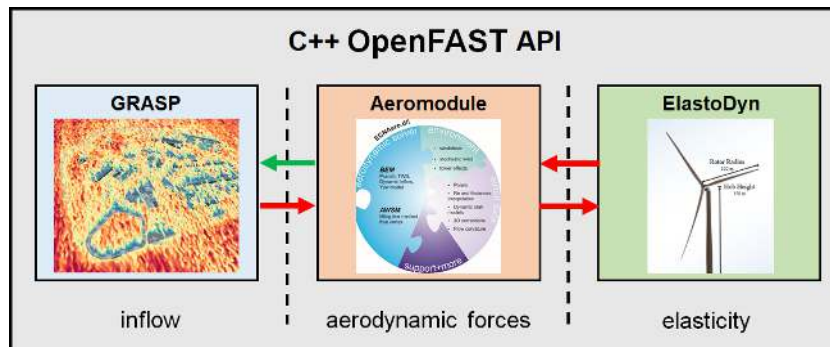
Figure 21: Sketch of the GRASP-OpenFAST-AM coupling for a simple case with ElastoDyn and AM. The green arrow highlights the additional information flow when the two-way AL coupling is activated.

3.3　Two-way coupling verification case

A simple case has been considered for preliminary verification of the two-way coupling. The case has been taken from Martinez et al. [13], who compared the results of four different LES AL codes, namely SOWFA [29], EllipSys [46, 47], SP-Wind [48, 49] and LESGO [50]. The comparison was performed on a rigid version of the NREL5MW reference wind turbine [51] rotating at a constant speed of 9.155 rpm with a wind speed of 8 m/s (corresponding to a tip speed ratio of 7.55 and a thrust coefficient around 0.8).

The same case has been replicated using GRASP-OpenFAST, where ElastoDyn has been used to model the rigid turbine and both AeroDyn (OpenFAST's aerodynamic module) and AM have been used for the aerodynamic calculations. Due to the simplicity of the case, the two aerodynamic solvers found very similar results so only the former are reported in the plots below. The uniform inflow velocity of $U_\infty = 8$ m/s has been prescribed without any turbulence at the inlet, and the side boundary conditions have been set periodic. In GRASP simulations, the mesh resolution has been set to 2.6 m to fit in the GPU memory, while in the other simulations, the cell size was 2 m. The mesh resolution corresponds to 50 cells along the diameter ($D/dx = 50$). A constant time step of 0.04 s is used for both GRASP and OpenFAST. The domain is large, 24 D in streamwise and 6 D in spanwise directions, to minimize the effect of boundary conditions. Standard Smagorinsky subgrid scale model is used for the unresolved turbulence.

Figure 22 shows the time-averaged quantities along the rotor blades. The agreement in the angle of attack and axial velocity is excellent. The aerodynamic coefficients show discontinuous behavior for SOWFA, SP-Wind and LESGO, which is related to the abruptly changing airfoil data. GRASP and EllipSys smooth the data, and therefore, the coefficients do not show similar unrealistic discontinuities. GRASP shows a slight overprediction for drag towards the blade tip, but generally, the agreement of GRASP to the other solvers is good.

The forces from the AL model are projected to the LES grid and the resulting wake is shown in fig. 23, which shows the mean velocity field with the different solvers. Close to the rotor, the wakes are similar among all solvers, but further downstream, the vortex breakdown and the development of turbulence in the wake are predicted differently. The turbulent transition is well visible in the first component of the Reynolds stress tensor $\overline{u'u'}/U_\infty^2$ field in fig. 24. Before the transition, the magnitude is close to zero, and further downstream, the stress increases rapidly,
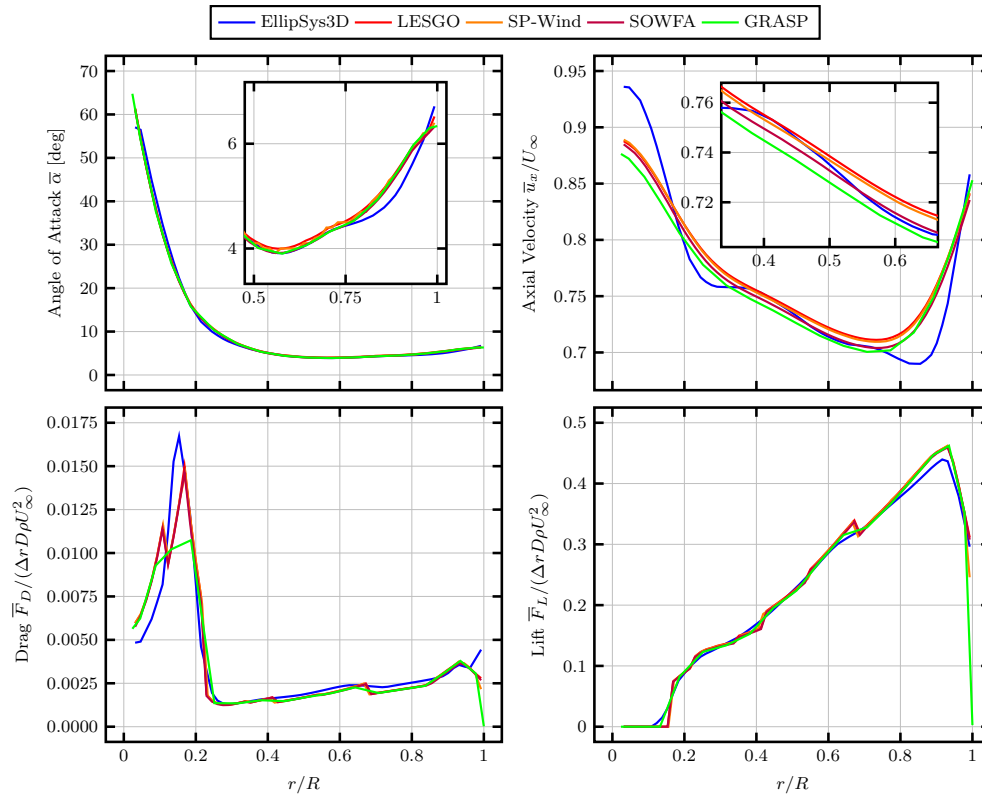
Figure 22: Comparison of the angle of attack, axial velocity, lift and drag along the blade.

which is where the transition occurs. After the transition, the mean velocity becomes relatively uniform (fig. 23) because of the turbulence that enhances the mixing. SP-Wind and LESGO with high-order pseudo-spectral method predict an earlier transition, while SOWFA and EllipSys predict delayed transition with their lower order finite volume method. The numerical diffusion introduced by the second-order upwind advection scheme used in SOWFA and EllipSys stabilizes the flow. The present GRASP simulation uses a finite difference method with a second-order central scheme for advection. The scheme's numerical dissipation and accuracy are between the pseudo-spectral and finite volume methods. Therefore the results are also consistent with the wake transitioning between the two methods. The magnitude of the Reynolds stress $\overline{u'u'}/U_\infty^2$ of GRASP is lower than the other solvers, as expected with a coarser computational grid that resolves less turbulent length scales in LES.
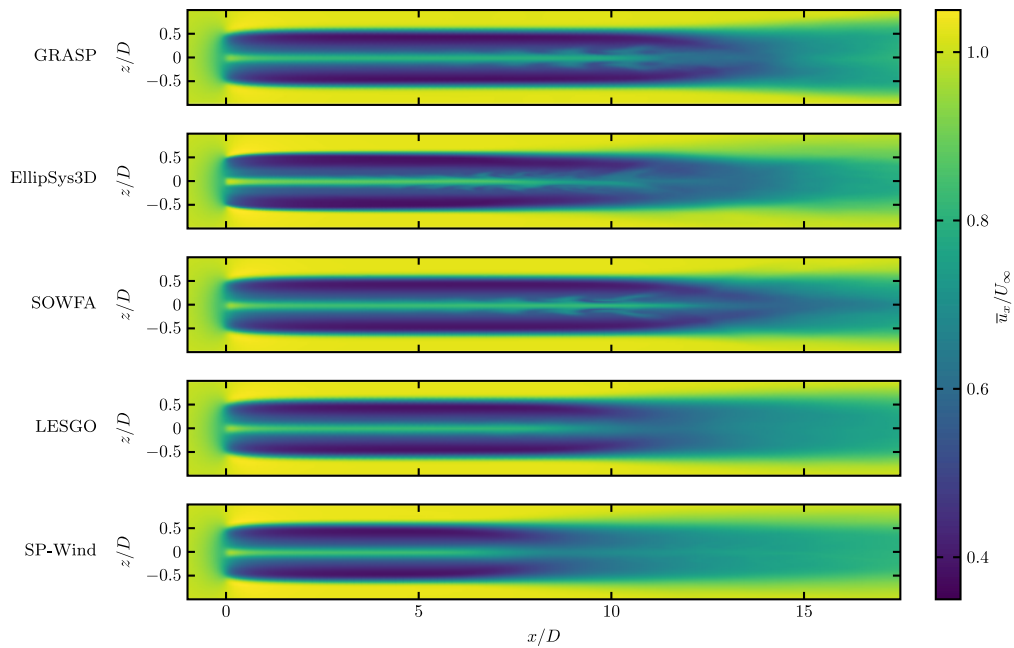
Figure 23: Comparison of the mean velocity U_X/U_∞ on a plane normal to cross-stream direction at turbine height.
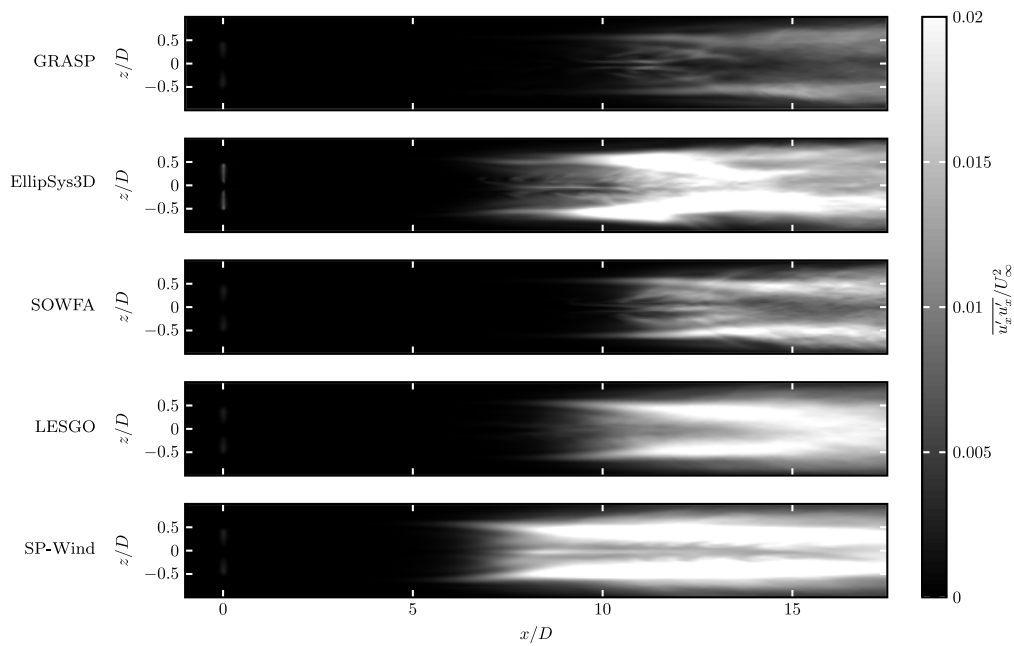
Figure 24: Comparison of the Reynolds stress $\overline{u'u'}/U_\infty^2$ on a plane normal to cross-stream direction at turbine height.

4   LES grid size sensitivity study

A sensitivity study investigating the effect of the ABL LES mesh resolution on several quantities of interest for aeroelastic load calculations has been carried out, and the main results are presented in this chapter. The sensitivity of the inflow parameters, which are output by GRASP, is first investigated in Section 4.1. Then, the corresponding turbine quantities calculated with the GRASP-OpenFAST-AM coupled tool are considered in Section 4.2.

The Østerlid canonical cases already presented in Section 2.6 have been used for this analysis since the previous ABL LES validation performed by Peña et al. [26] has allowed reducing the uncertainty in the numerical setup. Choosing Østerlid has also given the possibility to consider the three idealized ABL stability conditions (neutral, stable, and unstable) while minimizing the risk of site-specific effects in the results thanks to the quasi-canonical homogeneous flow that characterizes the site.

The results for all grids and stability conditions have been obtained following the same workflow: first, a standalone GRASP simulation was run to let the ABL develop; once a well-developed profile was reached, the GRASP-OpenFAST-AM interface was activated running the aeroelastic calculations for an additional hour of simulation with an online one-way coupled approach (see Chapter 3). Unless specified differently, all the quantities plotted in this chapter have been extracted from this last simulated hour.

This chapter presents the whole set of simulations performed summarizing the main results of this sensitivity study. A separate publication will present the numerical setup and discuss the most interesting results in greater detail, focusing on the neutral ABL case.

4.1   Sensitivity of flow parameters to the cell size of the LES grid

The GRASP setup for the idealized cases of Østerlid has already been described in Section 2.6. The same input settings, domain size, SGS model, and numerical schemes have been used in this sensitivity analysis, adjusting the LES mesh characteristics only. The four meshes described in Table 1 have been considered. All these grids consist of uniform cubic cells that can be fully described by their characteristic length. Having used an adjustable time step based on a maximum allowed Courant number of 0.8, the required link between temporal and spatial resolutions was always respected.

Table 1: Summary of the geometric characteristics of the four grids generated in this work. All grids have the same cuboid external domain with constant longitudinal, lateral and vertical sizes. The grid domains were discretized with cubic cells having sizes ranging from 32m to 4m.

grid	$X = Y$ [m]	Z [m]	$\Delta X = \Delta Y = \Delta Z$ [m]
32m	1024	2048	32
16m	1024	2048	16
8m	1024	2048	8
4m	1024	2048	4

The selected cell dimensions ranged from 32m to 4m, aligning with the suggestions given in previous works on ABL LES (e.g. [6, 28, 52, 53]). The resulting grids were all finer than the ones described in Section 2.6 reflecting the need to resolve smaller scales when inflow quantities that are relevant to load calculations are to be considered (see Chapter 1). Unfortunately, an ulterior grid refinement could not be achieved due to limits in the computational resources available.

The vertical profiles of the longitudinal and horizontal wind speed and wind direction obtained with the different meshes for the neutral, stable, and unstable conditions are depicted in fig. 25, 26, and 27, respectively. The horizontal wind speed is the resultant of the longitudinal (along x) and lateral (along y) wind speed components, while the wind direction is the angle between the horizontal wind speed and the longitudinal direction. Note that next to each plot showing the distribution of a quantity over the entire domain height, a zoomed view in the region of interest for typical wind turbine rotors is depicted. The bars superimposed on the mean vertical profiles indicate the standard deviations. All figures refer to the last hour of simulated time for each ABL stability case (the same for all the grids): from the 11th to the 12th hour for the neutral case; from the 16th to the 17th for the stable case; and from the 7th to the 8th for the unstable one (in which the greater mixing induced by the surface heat fluxes speeds up the inflow development).

Figure 25: Simulated vertical profiles of the longitudinal wind speed, horizontal wind speed (resultant of the longitudinal and lateral wind speed) and wind direction (angle between the horizontal wind speed and the longitudinal direction) for neutral conditions. Error bars depict ±1 standard deviation from the mean.
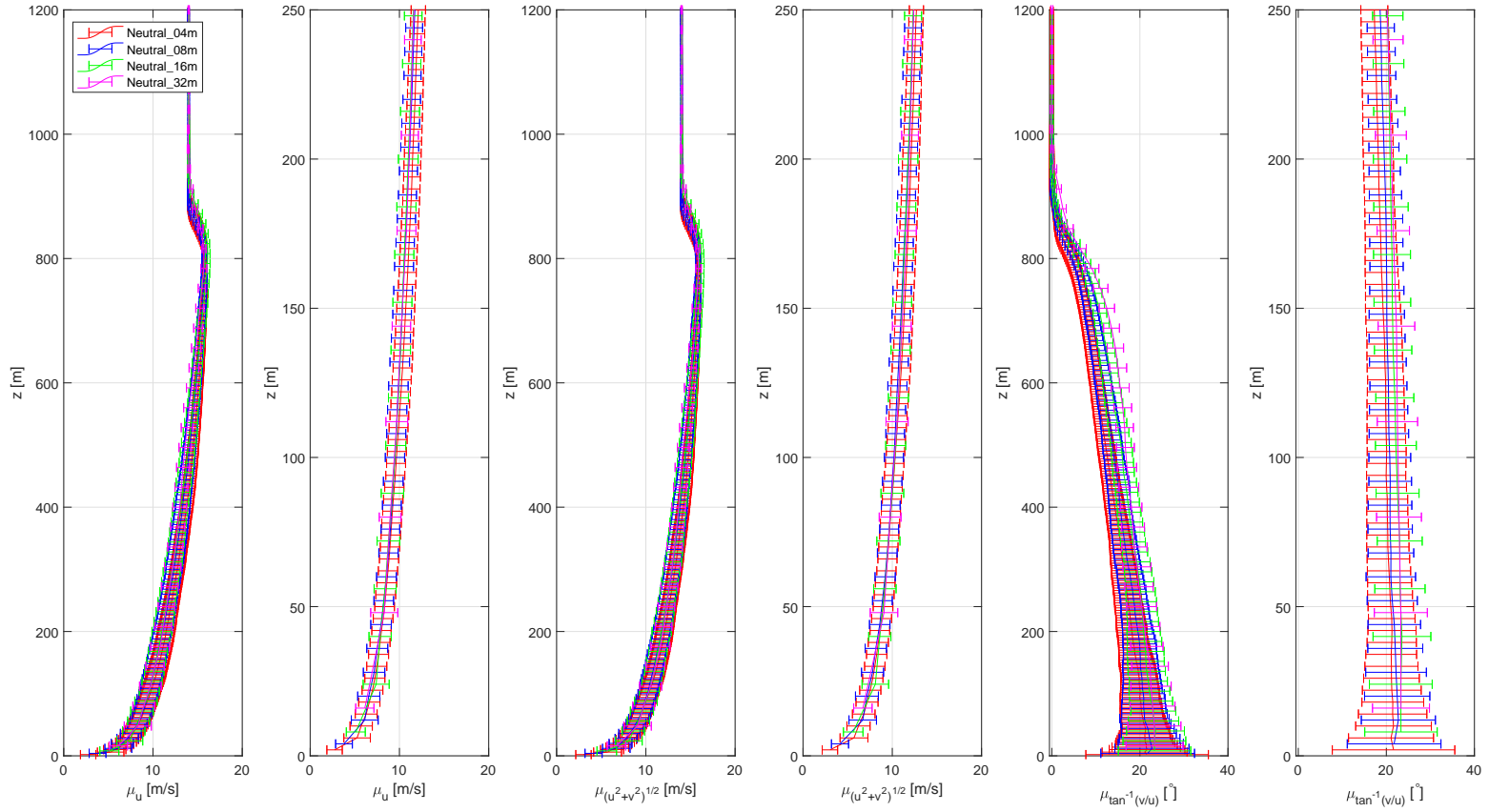
Figure 26: Simulated vertical profiles of the longitudinal wind speed, horizontal wind speed (resultant of the longitudinal and lateral wind speed) and wind direction (angle between the horizontal wind speed and the longitudinal direction) for stable conditions. Error bars depict ±1 standard deviation from the mean.
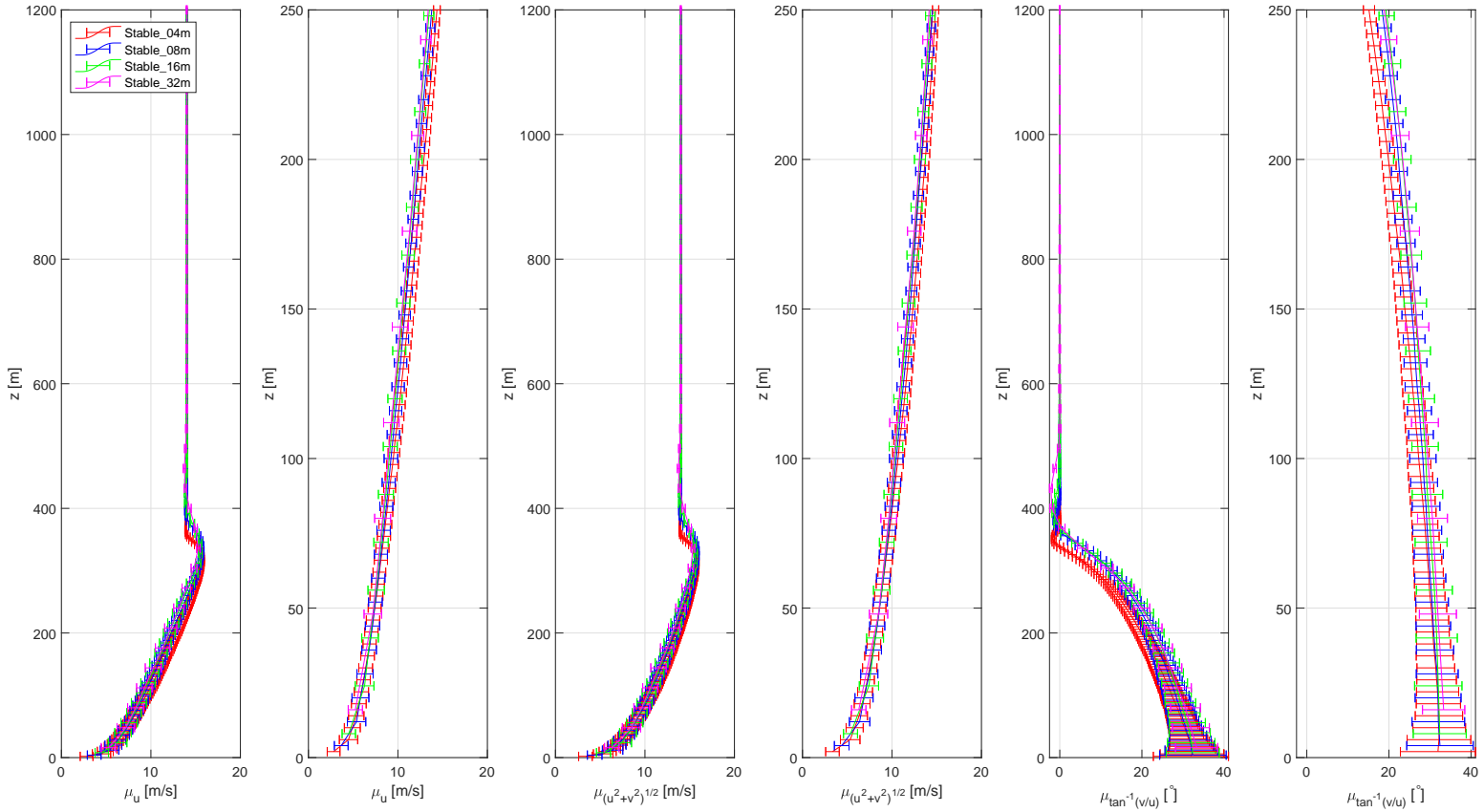
Figure 27: Simulated vertical profiles of the longitudinal wind speed, horizontal wind speed (resultant of the longitudinal and lateral wind speed) and wind direction (angle between the horizontal wind speed and the longitudinal direction) for unstable conditions. Error bars depict ± 1 standard deviation from the mean.
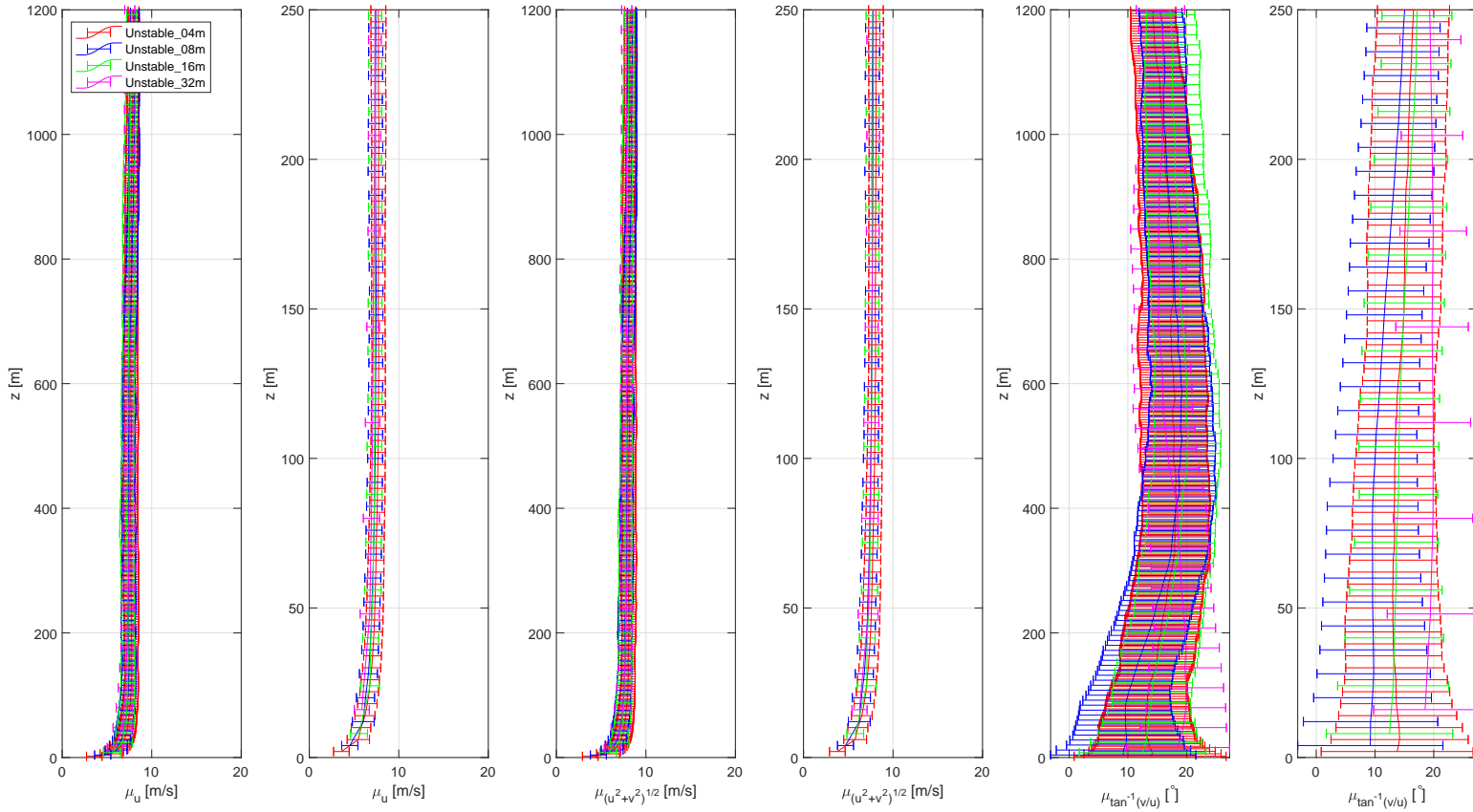
In general, the vertical profiles of the mean wind speed and direction obtained with the different meshes and stability conditions show similar differences to those observed in previous works [6, 52, 53, 54]. Slightly larger variability can be found for the wind direction, especially in the unstable case (fig. 27). The standard deviations of all the quantities investigated are very similar for the different grids.

From a site-assessment point of view, the differences among the grids are not significant, but the same cannot be said when it comes to aeroelastic load calculations. The zoomed views help highlight differences in the rotor plane region, and a close look reveals discrepancies of about 1m/s for the mean wind speed, and up to 5deg for the mean wind direction among the different meshes. Similar values have a significant impact on the mean aerodynamic loads on the blades and therefore affect the aeroelastic response of a wind turbine. The lack of a quantitative and universally accepted grid convergence metric was already pointed out in [54] for stable ABL conditions. Based on the present results the authors would add that, if ABL LES are to be used for load calculations, strict requirements in terms of mean wind profiles match would be needed.

The observed differences in the mean flow quantities would likely reduce if longer (multi-hour) time windows are considered for the statistics. In fact, wind speed variations may have important components at periods larger than 1h affecting the comparison. However, longer windows do not suit the intervals needed for aeroelastic load calculations that are only 10min-long, and would further increase the already significant computational burden. Hence, the ability to target specific hub height mean flow conditions with ABL LES is identified as a key feature to increase the attractiveness of this tool for wind turbine design load calculations. Due to the strong non-linear coupling terms in the Navier-Stokes equations, the development of LES flow control techniques is a complex matter that requires further research [32].

Another consequence of using a 1h time window is that the grid comparison results are also sensitive to which simulated hour is considered for the statistics. Figure 28 shows the time history of the longitudinal velocity component at an example height of 103m (the same used in [26]) for the different grids and stability conditions tested. It can be noticed that even after the initial transient period there is some variability in the mean flow, especially for the neutral and unstable ABL conditions (as expected). This uncertainty adds to the difficulties of assessing the quality of the different mesh results in terms of average inflow quantities.

Looking at the turbulence characteristics in the frequency domain allows disregarding the discrepancies observed in the vertical wind profiles (fig. 29). The Power Spectral Densities of the longitudinal velocity component at the same 103m height considered above are plotted for the different grids and stability conditions. To compare with the results from Peña et al. [26], the PSDs have been obtained by dividing the last simulated hour into 51 ten-minute intervals, each with a 540s overlap, and ensemble averaging the corresponding spectra. To obtain the same frequency bins for different meshes, all the signals have been resampled at 1Hz.

The comparison with the Weather Research and Forecasting (WRF) LES software results from [26] shows a very good agreement with respect to the 16m GRASP grid at the higher frequencies, whereas a slightly larger energy content is found by GRASP at the lower harmonics. The good agreement with the 16m grid is not surprising, as the lateral dimensions of the cells used in [26] were 15m long and the vertical dimension was stretched from 5m at the lowest level to 32m at the top domain boundary. Since different LES solvers were used, featuring different discretization schemes, SGS filter models, and cell geometries, the match between GRASP and WRF results
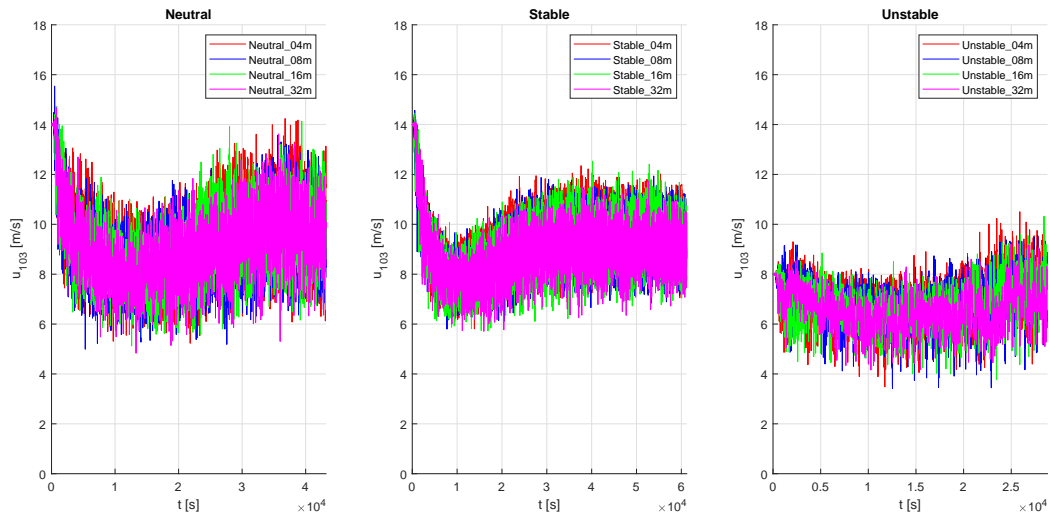
Figure 28: Simulated longitudinal and lateral wind speeds at 103 m above the ground as a function of time for neutral conditions.
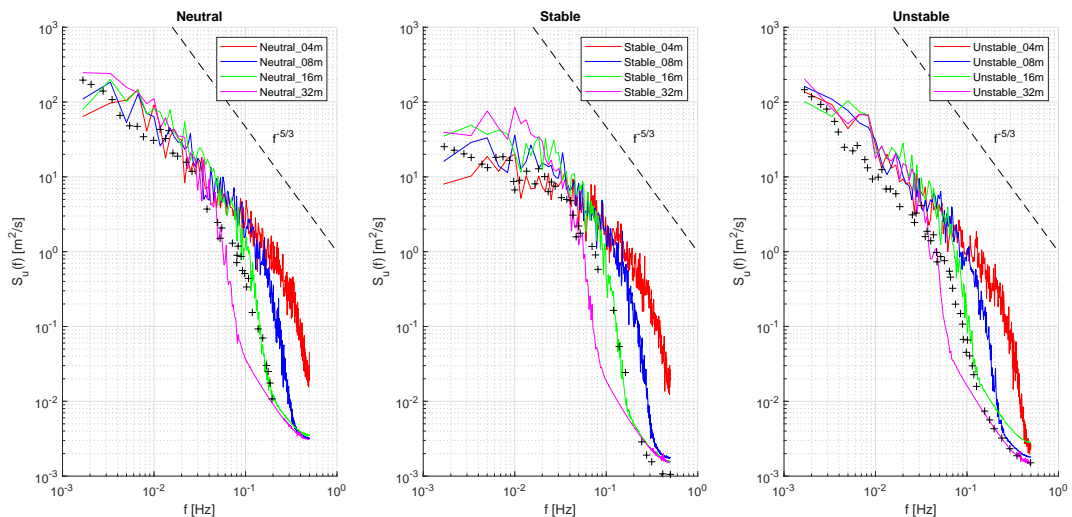
Figure 29: PSD of the longitudinal velocity component at 103m height for the different grids and stability conditions. The + marks in black denote the WRF results from [26]

may be considered good. Except for the lowest frequency range in the stable case showing a larger variability, the GRASP results from the different grids are in good agreement with each other up to the filter cutoff frequency, before which they all follow the Kolmogorov slope. As expected, refining the grid shifts the cut-off threshold to higher frequencies resulting in a larger portion of the energy cascade being resolved.

4.2   **Sensitivity of wind turbine rotor quantities to the cell size of the LES grid**

During the last hour of the simulated time, the GRASP-OpenFAST-AM coupling was used to study the sensitivity of some key turbine aeroelastic quantities to the LES mesh resolution. The same special onshore version of the IEA 15MW reference wind turbine (240m diameter, 150m hub height [55]) developed for the comparison of aeroelastic results within the IEA Task 47 [56] has been considered. Such a large rotor has been chosen to be representative of the state of the art of offshore wind turbines. Considering its simplified onshore version, specifically devised for aeroelastic results comparison, has allowed minimizing the uncertainty in the aeroelastic model description while matching the choice of Østerlid (onshore) as a reference site.

The aeroelastic calculations have been run with the online one-way coupling (see Chapter 3) for the last simulated hour to obtain six ten-minute realizations, which approximate the IEC 61400-1 [15] requirement of considering six different synthetic turbulence generator seeds. The inflow characteristics obtained with the different grids for this interval have already been presented in Section 4.1, and only the OpenFAST-AM outputs are discussed here.

The ElastoDyn module (ED) was used as the structural solver including all available blade and tower modes. The drivetrain flexibility and the shaft tilt angle have been neglected. To simplify the comparison among the different grids, the blade pitch angle, the rotor speed, and the nacelle yaw angle have been prescribed based on the mean wind vector at hub height for each stability condition. Table 2 reports the values prescribed for the different cases. The aerodynamic calculations have been performed using AM's blade element momentum solver using a constant time step, common to both AM and ED modules, of 0.02s.

Table 2: Prescribed turbine operating conditions for the different ABL stability cases tested.

	Ω [rpm]	θ_{Pitch} [deg]	Ψ_{Yaw} [deg]
Neutral	7.5	2.8	20.25
Stable	7.5	5.5	25.3
Unstable	5.7	0.0	13.85

Figure 30 depicts the spanwise distributions of the mean and standard deviation of normal and tangential aerodynamic forces for the three ABL cases considered. As expected, the mean values show significant discrepancies for the different grids due to the mean inflow differences found in Section 4.1. The mean aerodynamic forces are extremely sensitive, indeed, to the mean wind speed and direction because of their non-linear dependency on the effective wind vector at each radial location.

Figure 30: Spanwise distributions of the mean chord-normal (above) and chord-tangential (below) aerodynamic unit forces for the different meshes and stability conditions tested. The error bars depict ±1 standard deviation from the mean values.
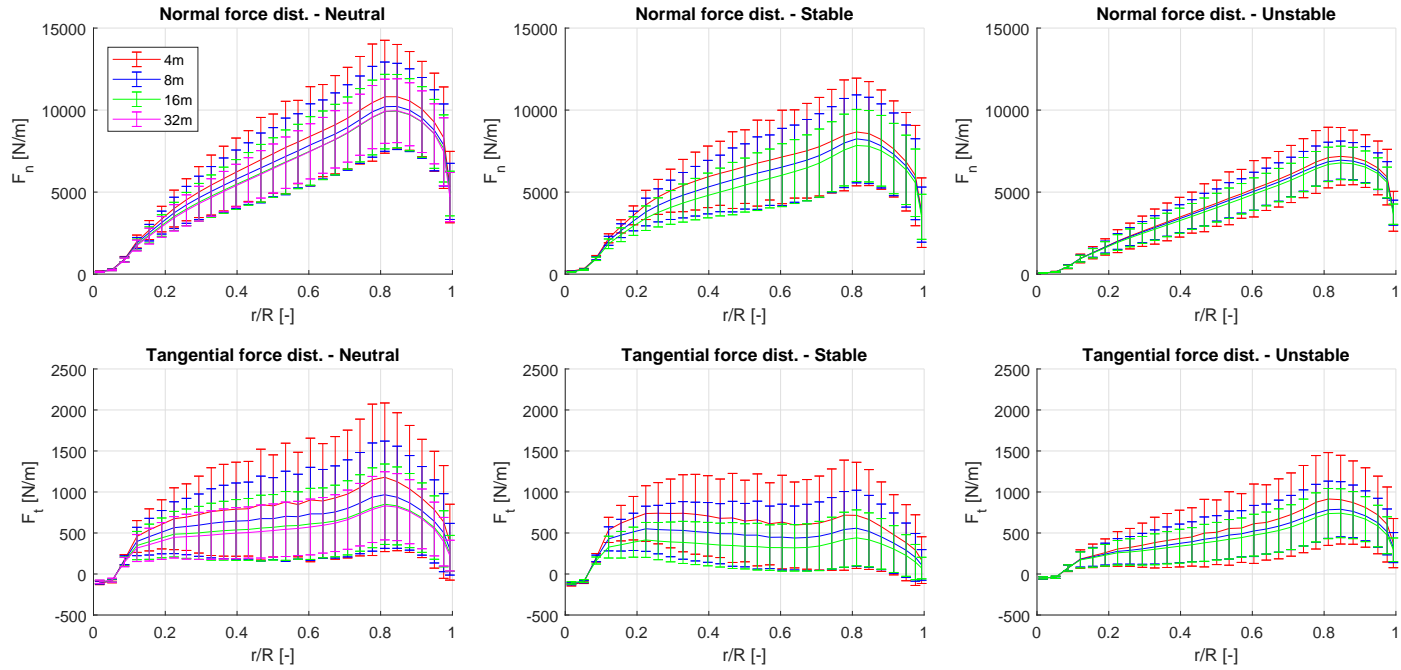
A more interesting evidence is the pronounced increase of the force standard deviations as more refined meshes are considered. This occurs for all ABL stability conditions tested. Unlike the mean value differences, this effect can hardly be explained by discrepancies in the standard deviation of the main inflow quantities, which have been shown to be quite consistent between the grids for all cases (Section 4.1). The main hypothesis for this trend is that it results from the different spatial discretizations affecting the rotational sampling of the turbulence. In fact, the redistribution of energy across the frequency bins in the rotational spectrum [24] increases the harmonic content especially around 1P, 2P, and 3P where the energy is still high enough to contribute significantly to the standard deviation of the rotationally sampled wind.

To verify this hypothesis, the spectrum of the axial component (i.e. normal to the rotor plane) of the wind rotationally sampled by a blade aerodynamic control point located at approximately 80% of the span has been depicted in fig. 31. The power spectral densities have been obtained with Welch's method to reduce the noise and aid their interpretability. Apart from the 1P peak, which is also very much affected by non-uniformities in the inflow (e.g. wind shear, veer, and rotor-inflow misalignments) other than the rotational sampling contribution, the plots show an increase of the 2P and 3P peaks (except in the stable case where only the 2P increases) for the finer grids.

In neutral conditions, for example, the greater standard deviation for the 4m rather than the 8m grid arises from the higher energy content in the range between 2P and 2Hz, after which the energy level drops and the larger aliased harmonics have a negligible impact on the standard deviation. In unstable conditions the finest grid finds a higher energy content for the whole frequency range, but the reasons for such a broadband increase require further investigation.Note that, according to the IEC 61400-1 guidelines for synthetic turbulence generators, only the finest grid tested complies with the spatial resolution requirement set, which, for the IEA 15MW turbine rotor, corresponds to a maximum characteristic diagonal cell length of 10.5m and therefore a maximum edge of about 7.4m [15].

To further assess how the different grid resolutions affect the IEA 15MW turbine aeroelastic response, the flatwise and edgewise blade root bending moment spectra for the different meshes and conditions have been reported in fig. 32 (always relying on the Welch method for their estimation). The 1P peak is dominant in all the spectra. For the flatwise moment, this is mainly due to inflow non-uniformities. Whereas the edgewise moment is largely driven by the gravity. Up to this frequency no clear trends can be recognized comparing the results of different grids.

The blade root bending moment spectra, specially for the flatwise component, show similar peaks at 2P and 3P as those observed in the locally sampled wind spectra shown in fig. 31. The size of these peaks increases as the grids are refined. The neutral case plots clearly show how the 16m and the 32m plots are not capable of capturing the rotational sampling effect appropriately. The 8m grid, which is close to the minimum threshold prescribed by the standard, lacks a bit of energy but goes closer to the 4m predictions.

However, the flatwise spectra highlight the presence of two other peaks at some blade natural frequencies (one around 0.7Hz and the other close to 2Hz) in all the conditions tested. While the energy content of the first peak is quite similar between the two finest grids, the size of the second one appears very sensitive to the grid resolution suggesting that a further grid refinement may still raise its energy content significantly. The latter peak lays above the filter cut-off frequencies of all grids indeed, and it would require finer meshes to be correctly captured. Due to computational

limits a finer mesh could not be tested in this work, but a further refinement is left as an important path to pursue in future works to verify the hypotheses discussed so far.

A less expensive alternative to model the complete aeroelastic response would be to enrich the high-frequency part of the LES wind spectrum, making sure that it follows Kolmogorov's law up to the smallest scales using artificial tricks like the fractal interpolation used in [27, 28], or similar. However, the characteristics of the turbulence generated with such hybrid techniques require further investigation and the challenges of implementing similar approaches in a coupled tool need to be tackled.

Figure 31: PSDs of the axial wind component (expressed in the rotor plane reference system) sampled at the quarter-chord point of an aerodynamic control element located at 80% of the span of blade 1 for the different meshes and stability conditions tested. The vertical lines highlight the rotational frequency and its multiples.
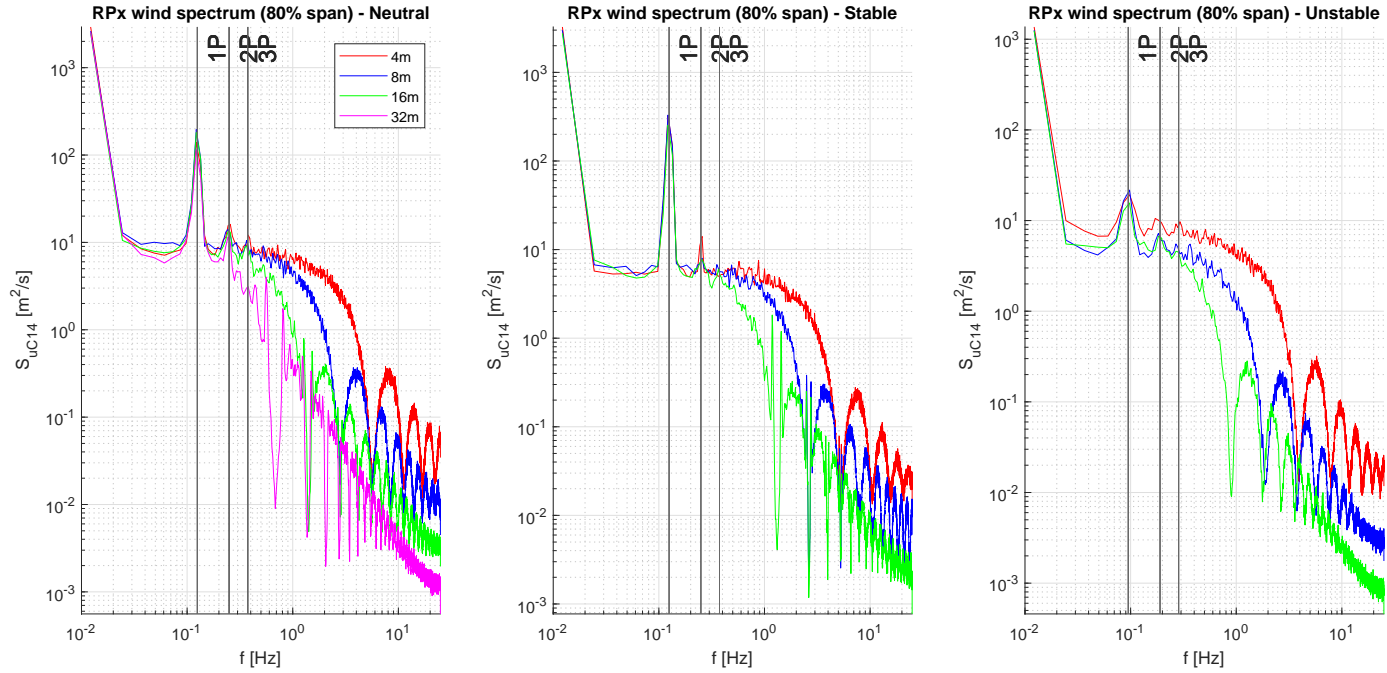
Figure 32: PSDs of the flatwise (above) and edgewise (below) blade 1 root bending moment for the different meshes and stability conditions tested. The vertical lines highlight the rotational frequency and its multiples.
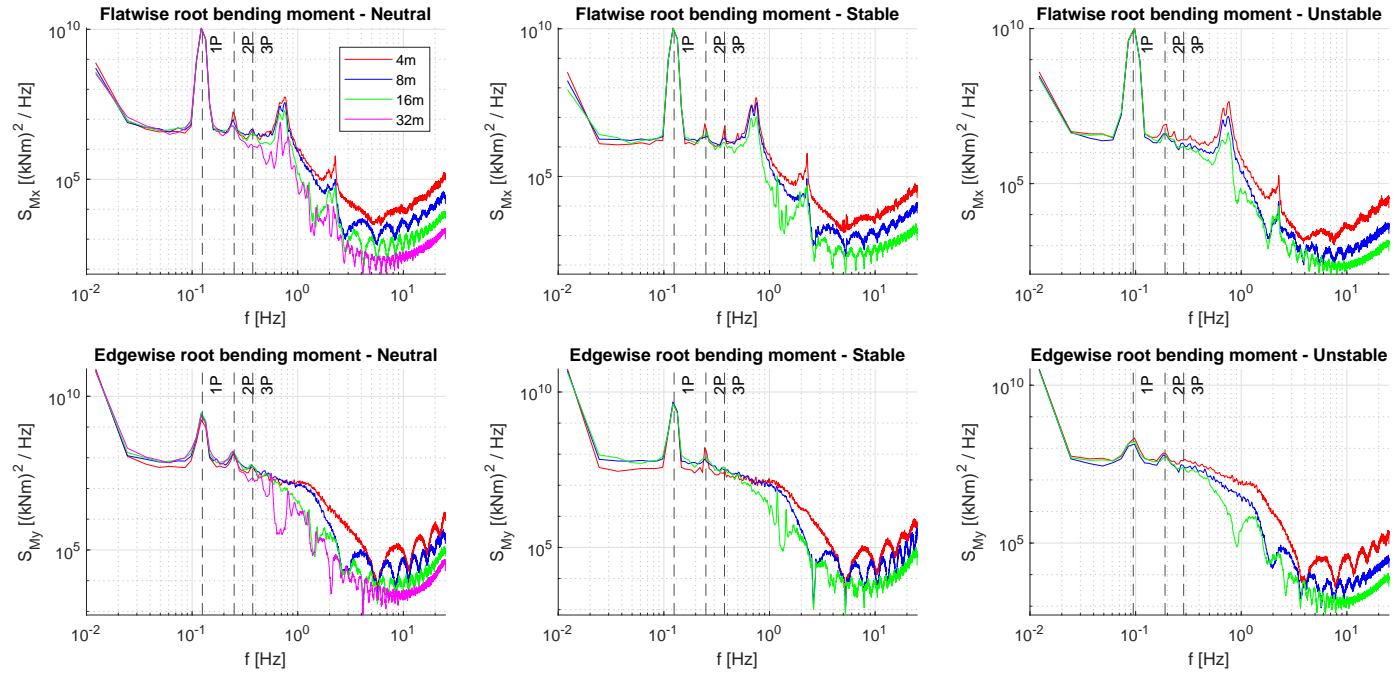
5　Conclusions

The present work has laid the groundwork for the use and validation of ABL LES in the context of wind turbine aeroelastic load calculations. The presented results contribute to tackling most of the challenges discussed in Chapter 1. Although many more are still outstanding, it is hoped that this study stimulates the scientific discussion speeding up the progress of research.

As a first step, turbine-relevant inflow quantities (mainly wind speed and TI) obtained with GRASP have been validated against met mast measurements available at different sites. A better agreement has been found for the IJmuiden offshore site than the onshore sites of Cabauw, Østerlid, and especially Rodeser Berg (because of the more complex terrain) which have shown larger discrepancies. In terms of wind speed, a maximum bias of about 0.6 m/s has been found in the worst case. Tuning the SGS filter based on stability parameters has further improved the wind speed match for the Cabauw site, and a similar benefit is expected for other onshore sites as well (although this needs to be proven in future work). For the TI, GRASP has been shown capable of capturing the shape of the histograms accurately though the exact TI values (especially at the lowest measurement heights) are very sensitive to the surface roughness assigned to the terrain, which is subject to high uncertainty when complex terrains are considered. A precise match has been anyhow found for the TI at higher heights (closer to typical wind turbine hub locations) and wind speeds (near and above rated), which are most influential for wind turbine operations. Overall, the good agreement between measurements and simulations has increased the confidence in using GPU-based ABL LES for realistic inflow generation at reasonable computational costs.

To enable efficient use of the LES inflow for aeroelastic load calculations, a coupling between GRASP and OpenFAST has been developed. The coupled tool allows the user to choose between a one-way coupling approach where the LES simulation is only used to generate the inflow and the turbine is not modelled, and an actuator line approach where the aerodynamic forces on the blades affect the LES wind field generating the wake. The first approach is convenient when load calculations on a single turbine have to be performed, whereas the actuator line method offers higher fidelity and can be used to study wake interactions and blockage effects on a farm. Both approaches support the use of TNO AeroModule as an alternative aerodynamic solver. For the actuator line coupling, a preliminary verification on a simple case has confirmed its current functioning and more extensive validation campaigns need to be carried out in future work. Nevertheless, the coupled tool developed in this project is already being used in other works (e.g. [57]) that will further contribute to its development and validation.

Finally, to prepare for the validation of LES-based aeroelastic load calculations on large wind turbines, a sensitivity study has been conducted to investigate the impact of the grid resolution used in LES on both inflow and aeroelastic quantities. The famous canonical flows at the Østerlid site presented by Peña et al. [26] have been selected for this task. The generated wind fields have been used to simulate the aeroelastic response of the IEA15MW reference wind turbine. The analysis confirmed the results to be sensitive to the LES cell size, not only at the SGS filter size frequencies where the expected drop of the energy content is found, but also at integer multiples of the rotor speed harmonic likely due to differences in the rotational sampling of the turbulence. The latter effect appears to fade away if the spatial discretization requirements specified in the IEC 61400-1 standard for synthetic turbulence generators are respected.

TNO PUBLIC

5.1   Future work

Several open challenges still remain to be tackled. The first, which has not been addressed in this work, is looking for ways to control turbine-relevant inflow quantities in ABL LES so to facilitate the targeting of specific wind conditions of interest (e.g. hub-height wind speed, TI, shear exponent). This would allow LES to be more conveniently used in a conventional design process as an alternative to synthetic turbulence generators. Then, among the aspects covered in this report the following next steps have been identified:

- the inflow validation has indicated the need for a more detailed translation of terrain orographic properties into a surface roughness map for onshore sites that would improve the matching of TI. Moreover, the SGS filter tuning based on stability parameters, which has yielded very promising results for the Cabauw site, deserves further research and validation in more complex sites.

- the coupled tool requires an extensive validation campaign for both one-way and two-way (AL) coupling. This should consider different rotors and inflow properties, and compare GRASP-OpenFAST-AM results against measurements and simulations based on synthetic turbulent inflow.

- the scope of the sensitivity study should be extended to investigate the influence of other important LES parameters (e.g. SGS model, numerical schemes, etc.) on rotor-relevant quantities to come up with standard guidelines to be followed when setting up a simulation. Moreover, engineering methods to increase the high-frequency content of the LES turbulence spectrum without refining the mesh may be worth investigating, looking for a convenient trade-off between accuracy and computational costs.

6   Bibliography

[1]   D. Mehta et al. "Large Eddy Simulation of wind farm aerodynamics: A review." In: *Journal of Wind Engineering and Industrial Aerodynamics* 133 (2014), pp. 1–17. ISSN: 0167-6105. DOI: `https://doi.org/10.1016/j.jweia.2014.07.002`. URL: `https://www.sciencedirect.com/science/article/pii/S0167610514001391`.

[2]   F. T. M. Nieuwstadt and R. A. Brost. "The Decay of Convective Turbulence." In: *Journal of the Atmospheric Sciences* 43(6) (1986), pp. 532–546. DOI: `10.1175/1520-0469(1986)043<0532:TDOCT>2.0.CO;2`.

[3]   J. W. M. Cuijpers and P. G. Duynkerke. "Large Eddy Simulation of Trade Wind Cumulus Clouds." In: *Journal of the Atmospheric Sciences* 50(23) (1993), pp. 3894–3908. DOI: `10.1175/1520-0469(1993)050<3894:LESOTW>2.0.CO;2`.

[4]   Jeff Mirocha, Branko Kosović, and Gokhan Kirkil. "Resolved Turbulence Characteristics in Large-Eddy Simulations Nested within Mesoscale Simulations Using the Weather Research and Forecasting Model." In: *Monthly Weather Review* 142.2 (2014), pp. 806–831. DOI: `10.1175/MWR-D-13-00064.1`. URL: `https://journals.ametsoc.org/view/journals/mwre/142/2/mwr-d-13-00064.1.xml`.

[5]   T. L. Burton et al. *Wind Energy Handbook, 3rd Edition*. Wiley, 2021. ISBN: 978-1-119-45109-9.

[6]   J. D. Mirocha et al. "Large-eddy simulation sensitivities to variations of configuration and forcing parameters in canonical boundary-layer flows for wind energy applications." In: *Wind Energy Science* 3.2 (2018), pp. 589–613. DOI: `10.5194/wes-3-589-2018`. URL: `https://wes.copernicus.org/articles/3/589/2018/`.

[7]   Richard J.A.M. Stevens and Charles Meneveau. "Flow Structure and Turbulence in Wind Farms." In: *Annual Review of Fluid Mechanics* 49.1 (2017), pp. 311–339. DOI: `10.1146/annurev-fluid-010816-060206`. eprint: `https://doi.org/10.1146/annurev-fluid-010816-060206`. URL: `https://doi.org/10.1146/annurev-fluid-010816-060206`.

[8]   Jens Nørkær Sørensen and Wen Zhong Shen. "Numerical Modeling of Wind Turbine Wakes." In: *Journal of Fluids Engineering* 124.2 (May 2002), pp. 393–399. ISSN: 0098-2202. DOI: `10.1115/1.1471361`. eprint: `https://asmedigitalcollection.asme.org/fluidsengineering/article-pdf/124/2/393/5678518/393\_1.pdf`. URL: `https://doi.org/10.1115/1.1471361`.

[9]   Jens N. Sørensen et al. "Simulation of wind turbine wakes using the actuator line technique." In: *Philosophical Transactions of the Royal Society A: Mathematical, Physical and Engineering Sciences* 373.2035 (2015), p. 20140071. DOI: `10.1098/rsta.2014.0071`. eprint: `https://royalsocietypublishing.org/doi/pdf/10.1098/rsta.2014.0071`. URL: `https://royalsocietypublishing.org/doi/abs/10.1098/rsta.2014.0071`.

[10] Hao Lu and Fernando Porté-Agel. "Large-eddy simulation of a very large wind farm in a stable atmospheric boundary layer." In: *Physics of Fluids* 23.6 (2011), p. 065101. DOI: `10.1063/1.3589857`.

[11] Pierre-Antoine Joulin et al. "The Actuator Line Method in the Meteorological LES Model Meso-NH to Analyze the Horns Rev 1 Wind Farm Photo Case." In: *Frontiers in Earth Science* 7 (2020). ISSN: 2296-6463. DOI: `10.3389/feart.2019.00350`. URL: `https://www.frontiersin.org/article/10.3389/feart.2019.00350`.

[12] Jessica Strickland. "Modeling Wakes and Blockage in Large-scale Wind Farms." English. PhD thesis. Netherlands: University of Twente, Dec. 2021. ISBN: 978-90-365-5267-7. DOI: `10.3990/1.9789036552677`.

[13] H. M. Johlas et al. "Large eddy simulations of floating offshore wind turbine wakes with coupled platform motion." In: *Journal of Physics: Conference Series* 1256.1 (July 2019), p. 012018. DOI: `10.1088/1742-6596/1256/1/012018`. URL: `https://doi.org/10.1088/1742-6596/1256/1/012018`.

[14] Paul Fleming et al. "Overview of FLORIS updates." In: *Journal of Physics: Conference Series* 1618.2 (Sept. 2020), p. 022028. DOI: `10.1088/1742-6596/1618/2/022028`. URL: `https://doi.org/10.1088/1742-6596/1618/2/022028`.

[15] *Wind energy generation systems - Part 1: Design requirements*. Standard. International Electrotechnical Commission, Apr. 2019.

[16] J. C. Kaimal and J. J. Finnigan. *Atmospheric Boundary Layer Flows: Their Structure and Measurement*. Oxford University Press, 1994. ISBN: 9780195062397.

[17] Jakob Mann. "The spatial structure of neutral atmospheric surface-layer turbulence." In: *Journal of Fluid Mechanics* 273 (1994), pp. 141–168. DOI: `10.1017/S0022112094001886`.

[18] D. Winkelaar. *SWIFT program for three-dimensional wind simulation : part 1: Model description and program verification*. Report ECN-R–92-013. ECN, 1992.

[19] Neil Kelley and B. Jonkman. "Overview of the TurbSim Stochastic Inflow Turbulence Simulator." In: (Jan. 2007). DOI: `10.2172/15020329`.

[20] Jennifer M. Rinker. "PyConTurb: an open-source constrained turbulence generator." In: *Journal of Physics: Conference Series* 1037 (June 2018), p. 062032. DOI: `10.1088/1742-6596/1037/6/062032`. URL: `https://doi.org/10.1088/1742-6596/1037/6/062032`.

[21] Antonio Segalini and Johan Arnqvist. "A spectral model for stably stratified turbulence." In: *Journal of Fluid Mechanics* 781 (2015), pp. 330–352. DOI: `10.1017/jfm.2015.502`.

[22] Abhijit Chougule et al. "Modeling Atmospheric Turbulence via Rapid Distortion Theory: Spectral Tensor of Velocity and Buoyancy." In: *Journal of the Atmospheric Sciences* 74.4 (2017), pp. 949–974. DOI: `10.1175/JAS-D-16-0215.1`. URL: `https://journals.ametsoc.org/view/journals/atsc/74/4/jas-d-16-0215.1.xml`.

[23] A. Chougule et al. "Simplification and Validation of a Spectral-Tensor Model for Turbulence Including Atmospheric Stability." In: *Boundary-Layer Meteorol* 167 (2018), pp. 371–397. DOI: `10.1007/s10546-018-0332-z`.

[24] A. Cuerva-Tejero et al. "Another look at rotational sampling of atmospheric turbulence with focus on the transference of energy from different frequency intervals of the Eulerian spectrum to the rotational spectrum." In: *Journal of Wind Engineering and Industrial Aerodynamics* 219 (2021), p. 104803. ISSN: 0167-6105. DOI: `https://doi.org/10.1016/j.jweia.2021.104803`. URL: `https://www.sciencedirect.com/science/article/pii/S0167610521002786`.

[25] G. Schepers et al. "Aeroelastic loads on a 10 MW turbine exposed to extreme events selected from a year-long large-eddy simulation over the North Sea." In: *Wind Energy Science* 6.4 (2021), pp. 983–996. DOI: `10.5194/wes-6-983-2021`. URL: `https://wes.copernicus.org/articles/6/983/2021/`.

[26] A. Peña, B. Kosović, and J. D. Mirocha. "Evaluation of idealized large-eddy simulations performed with the Weather Research and Forecasting model using turbulence measurements from a 250 m meteorological mast." In: *Wind Energy Science* 6.3 (2021), pp. 645–661.

[27] Chungwook Sim, Sukanta Basu, and Lance Manuel. "The Influence of Stable Boundary Layer Flows on Wind Turbine Fatigue Loads." In: Jan. 2009. DOI: `10.2514/6.2009-1405`.

[28] Chungwook Sim, Lance Manuel, and Sukanta Basu. "A Comparison of Wind Turbine Load Statistics for Inflow Turbulence Fields Based on Conventional Spectral Methods and Large Eddy Simulation." In: Jan. 2010. DOI: `10.2514/6.2010-829`.

[29] *SOWFA: Simulator fOr Wind Farm Applications*. NREL. URL: `https://www.nrel.gov/wind/nwtc/sowfa.html`.

[30] NREL. *OpenFAST: Open-source wind turbine simulation tool*. Version v3.1.0. Apr. 14, 2022. URL: `http://github.com/OpenFAST/OpenFAST/`.

[31] R. C. Storey, S. E. Norris, and J. E. Cater. "An actuator sector method for efficient transient wind turbine simulation." In: *Wind Energy* 18.4 (2015), pp. 699–711. DOI: `https://doi.org/10.1002/we.1722`. eprint: `https://onlinelibrary.wiley.com/doi/pdf/10.1002/we.1722`. URL: `https://onlinelibrary.wiley.com/doi/abs/10.1002/we.1722`.

[32] Astrid Nybø et al. "Evaluation of different wind fields for the investigation of the dynamic response of offshore wind turbines." In: *Wind Energy* 23.9 (2020), pp. 1810–1830. DOI: `https://doi.org/10.1002/we.2518`. eprint: `https://onlinelibrary.wiley.com/doi/pdf/10.1002/we.2518`. URL: `https://onlinelibrary.wiley.com/doi/abs/10.1002/we.2518`.

[33] Thijs Heus et al. "Formulation of and numerical studies with the Dutch Atmospheric Large-Eddy Simulation (DALES)." In: *Geoscientific Model Development Discussions* 3 (Feb. 2010). DOI: `10.5194/gmdd-3-99-2010`.

[34] Jerôme Schalkwijk et al. "High-Performance Simulations of Turbulent Clouds on a Desktop PC: Exploiting the GPU." In: *Bulletin of the American Meteorological Society* 93.3 (2012), pp. 307–314. DOI: `10.1175/BAMS-D-11-00059.1`. URL: `https://journals.ametsoc.org/view/journals/bams/93/3/bams-d-11-00059_1.xml`.

[35] Ciaran Gilbert et al. "Statistical post-processing of turbulence-resolving weather forecasts for offshore wind power forecasting." In: *Wind Energy* 23.4 (2020), pp. 884–897. DOI: `https://doi.org/10.1002/we.2456`. eprint: `https://onlinelibrary.wiley.com/doi/pdf/10.1002/we.2456`. URL: `https://onlinelibrary.wiley.com/doi/abs/10.1002/we.2456`.

[36] *ERA5*. `https://www.ecmwf.int/en/forecasts/datasets/reanalysis-datasets/era5`. Accessed: 2022-08-19.

[37] A. Peña. "Østerild: A natural laboratory for atmospheric turbulence." In: *Journal of Renewable and Sustainable Energy* 11.6 (2019), p. 063302. DOI: `10.1063/1.5121486`. eprint: `https://doi.org/10.1063/1.5121486`. URL: `https://doi.org/10.1063/1.5121486`.

[38] *Cabauw in-situ measurements*. URL: `https://www.knmi.nl/research/observations-data-technology/projects/cabauw-in-situ-measurements` (visited on 12/13/2022).

[39] J.P. Maureira Poveda and D.A.J. Wouters. *Wind Measurements at Meteorological Mast IJmuiden*. Report ECN-E–14-058. ECN, 2015.

[40] Emily Fennell. "Comparison of Onshore and Offshore Boundary Layers in the HARMONIE Model for Wind Energy Purposes." In: (May 2018).

[41] W. C. Skamarock, J. B. Klemp, et al. *A Description of the Advanced Research WRF Version 3*. Report NCAR/TN-475+STR. University Corporation for Atmospheric Research, 2008. DOI: 10.5065/D68S4MVH.

[42] Wybe Rozema et al. "Minimum-dissipation models for large-eddy simulation." In: *Physics of Fluids* 27.8 (2015), p. 085107. DOI: 10.1063/1.4928700. eprint: https://aip.scitation.org/doi/pdf/10.1063/1.4928700. URL: https://aip.scitation.org/doi/abs/10.1063/1.4928700.

[43] Luis A. Martínez-Tossas, Matthew J. Churchfield, and Stefano Leonardi. "Large eddy simulations of the flow past wind turbines: actuator line and disk modeling." In: *Wind Energy* 18.6 (2015), pp. 1047–1060. DOI: https://doi.org/10.1002/we.1747. eprint: https://onlinelibrary.wiley.com/doi/pdf/10.1002/we.1747. URL: https://onlinelibrary.wiley.com/doi/abs/10.1002/we.1747.

[44] K. Boorsma, F. Grasso, and J. Holierhoek. *Enhanced approach for simulation of rotor aerodynamic loads*. Tech. rep. ECN-M–12-003. Petten, Netherlands: ECN, Dec. 2011.

[45] S. Mancini and K. Boorsma. *Definition and verification of the new coupling between Aero-Module and OpenFAST*. Tech. rep. TNO 2022 R10058. Petten, Netherlands: TNO Wind Energy, Feb. 2022. URL: http://resolver.tudelft.nl/uuid:4de2ee7c-e506-4f8b-916b-ba5a504f0433.

[46] Jess A. Michelsen. *Basis3D - a Platform for Development of Multiblock PDE Solvers: β - release*. English. Vol. AFM 92-05. Technical University of Denmark, 1992.

[47] Niels N. Sørensen. "General purpose flow solver applied to flow over hills." English. Published 2003. PhD thesis. 1995.

[48] Johan Meyers and Pierre Sagaut. "Evaluation of Smagorinsky variants in large-eddy simulations of wall-resolved plane channel flows." In: *Physics of Fluids* 19.9 (2007), p. 095105. DOI: 10.1063/1.2768944. eprint: https://doi.org/10.1063/1.2768944. URL: https://doi.org/10.1063/1.2768944.

[49] Johan Meyers and Charles Meneveau. "Large Eddy Simulations of Large Wind-Turbine Arrays in the Atmospheric Boundary Layer." In: *48th AIAA Aerospace Sciences Meeting Including the New Horizons Forum and Aerospace Exposition*. DOI: 10.2514/6.2010-827. eprint: https://arc.aiaa.org/doi/pdf/10.2514/6.2010-827. URL: https://arc.aiaa.org/doi/abs/10.2514/6.2010-827.

[50] *LESGO is a parallel pseudo-spectral large-eddy simulation code*. URL: https://lesgo.me.jhu.edu/ (visited on 07/04/2022).

[51] J. Jonkman, W. Musial S. Butterfield, and G. Scott. "Definition of a 5-MW Reference Wind Turbine for Offshore System Development." In: *NREL/TP-500-38060* (2009).

[52] H. Wurps, G. Steinfeld, and S. Heinz. "Grid-Resolution Requirements for Large-Eddy Simulations of the Atmospheric Boundary Layer." In: *Boundary-Layer Meteorology* 175 (2020), pp. 179–201. ISSN: 1573-1472. DOI: 10.1007/s10546-020-00504-1. URL: https://doi.org/10.1007/s10546-020-00504-1.

[53] Peter Sullivan and Edward Patton. "The Effect of Mesh Resolution on Convective Boundary Layer Statistics and Structures Generated by Large-Eddy Simulation." In: *Journal of Atmospheric Sciences* 68 (Oct. 2011), pp. 2395–2415. DOI: 10.1175/JAS-D-10-05010.1.

[54] B. Maronga and D. Li. "An Investigation of the Grid Sensitivity in Large-Eddy Simulations of the Stable Boundary Layer." In: *Boundary-Layer Meteorology* 182 (2022), pp. 251–273. ISSN: 1573-1472. DOI: 10.1007/s10546-021-00656-8. URL: https://doi.org/10.1007/s10546-021-00656-8.

[55] E. Gaertner, J. Rinker, et al. *Definition of the IEA 15-Megawatt Offshore Reference Wind*. Report NREL/TP-5000-75698. National Renewable Energy Laboratory, 2020.

[56] *IEA Wind TCP Task 47: Innovative Aerodynamic Experiments and Simulations on Wind Turbines in Turbulent Inflow*. IEA Wind. URL: https://iea-wind.org/task47/.

[57] Emanuel Taschner. "A new coupling of a GPU-resident large-eddy simulation code with a multi-physics wind turbine simulation tool." In: Presented at NAWEA/WindTech 2022 University of Delaware, USA, 2022.